Monthly Notices
of the
ROYAL ASTRONOMICAL SOCIETY

MNRAS **491,** 6045–6064 (2020)
Advance Access publication 2019 December 11

doi:10.1093/mnras/stz3464

On reverberation mapping lag uncertainties

Z. Yu [1]★ C. S. Kochanek,[1,2] B. M. Peterson,[1,2,3] Y. Zu [4] W. N. Brandt,[5,6,7] E. M. Cackett,[8] M. M. Fausnaugh[9] and I. M. McHardy[10]

[1]*Department of Astronomy, The Ohio State University, Columbus, OH 43210, USA*
[2]*Center of Cosmology and Astro-Particle Physics, The Ohio State University, Columbus, OH 43210, USA*
[3]*Space Telescope Science Institute, 3700 San Martin Drive, Baltimore, MD 21218, USA*
[4]*Department of Astronomy, School of Physics and Astronomy, Shanghai Jiao Tong University, Shanghai 200240, China*
[5]*Department of Astronomy and Astrophysics, Eberly College of Science, The Pennsylvania State University, 525 Davey Laboratory, University Park, PA 16802, USA*
[6]*Department of Physics, The Pennsylvania State University, 104 Davey Laboratory, University Park, PA 16802, USA*
[7]*Institute for Gravitation and the Cosmos, The Pennsylvania State University, University Park, PA 16802, USA*
[8]*Department of Physics and Astronomy, Wayne State University, 666 W. Hancock St, Detroit, MI 48201, USA*
[9]*Kavli Institute for Space and Astrophysics Research, Massachusetts Institute of Technology, 77 Massachusetts Avenue, Cambridge, MA 02139–4307, USA*
[10]*University of Southampton, Highfield, Southampton SO17 1BJ, UK*

Accepted 2019 December 5. Received 2019 December 4; in original form 2019 September 4

ABSTRACT

We broadly explore the effects of systematic errors on reverberation mapping lag uncertainty estimates from JAVELIN and the interpolated cross-correlation function (ICCF) method. We focus on simulated light curves from random realizations of the light curves of five intensively monitored AGNs. Both methods generally work well even in the presence of systematic errors, although JAVELIN generally provides better error estimates. Poorly estimated light-curve uncertainties have less effect on the ICCF method because, unlike JAVELIN, it does not explicitly assume Gaussian statistics. Neither method is sensitive to changes in the stochastic process driving the continuum or the transfer function relating the line light curve to the continuum. The only systematic error we considered that causes significant problems is if the line light curve is not a smoothed and shifted version of the continuum light curve but instead contains some additional sources of variability.

Key words: galaxies: nuclei – quasars: general.

1 INTRODUCTION

The masses of supermassive black holes (SMBHs) are critical to understanding active galactic nuclei (AGNs), their evolution and their effect on host galaxies. In nearby normal galaxies, direct SMBH mass measurements can be made using the kinematics of stars (e.g. van der Marel 1994; Gebhardt & Thomas 2009) or gas (e.g. Harms et al. 1994; Barth et al. 2016). These techniques require both high spatial resolution to resolve the black hole's region of influence and that the accretion activity is low enough to allow observations of the stars and gas. This restricts these measurements to nearby, inactive or mildly active galaxies. In AGNs, the reverberation mapping (RM) technique provides an approach to measuring the black hole mass using variability. Without the need for spatial resolution, RM allows SMBH mass measurements in active galaxies at (in principle) any distance.

RM follows the response of the broad-line region (BLR) emission lines to the variations in the continuum emission from the accretion disc. We can express the relation between the emission line and the continuum variations using a 'transfer function'[1] $\Psi(v, \tau)$ for the response of the line emission with line-of-sight velocity v after a time delay τ from a change in the continuum. Resolving the velocity dependence of $\Psi(v, \tau)$ requires high cadence and signal-to-noise data (e.g. Blandford & McKee 1982; Horne et al. 2004), so most RM studies consider only a 1D 'delay map' $\Psi(\tau)$ for the overall response of the line. In a linear echo model, the emission-line light curve is

$$L(t) = L_0 + \int \Psi(\tau)\, \Delta C(t-\tau)\, \mathrm{d}\tau \tag{1}$$

where L_0 is a constant that depends on the non-varying continuum level, $\Psi(\tau)$ is the transfer function, and $\Delta C(t-\tau)$ is the varying component of the continuum. The mean (centroid) time lag

$$\langle \tau \rangle = \frac{\int_0^\infty t\Psi(t)\, \mathrm{d}t}{\int_0^\infty \Psi(t)\, \mathrm{d}t} \tag{2}$$

[1] $\Psi(v, \tau)$ is also referred as the 'response function', depending on whether it is weighted by emissivity or responsivity. It is not critical to distinguish between these terms for this paper, so we only use the term 'transfer function' here.

★ E-mail: yu.2231@osu.edu

is then related to the black hole mass by

$$M_{\rm BH} = \frac{f c \langle \tau \rangle \Delta v^2}{G} \quad (3)$$

where f is a dimensionless 'virial factor' determined by the structure and kinematics of the BLR and Δv is the width of the broad emission line.

In addition to RM studies of emission-line lags, continuum RM studies measured the lags between different wavelengths of the continuum. The standard thin accretion disc model is hottest near the centre and colder at larger radii (e.g. Shakura & Sunyaev 1973; Shields 1978). If the continuum variability is driven by variable irradiation from the central regions, variability at longer wavelength will lag that at shorter wavelength. The continuum lag therefore encodes the size of the accretion disc as a function of temperature. Continuum RM studies have yielded lag measurements from both intensively monitored nearby AGNs (e.g. Shappee et al. 2014; Edelson et al. 2015; Fausnaugh et al. 2016; Cackett et al. 2018; McHardy et al. 2018) and more distant objects from large sky surveys (e.g. Jiang et al. 2017; Mudd et al. 2018; Homayouni et al. 2018; Yu et al. 2019).

Various algorithms have been used to estimate lags, such as the interpolated cross-correlation function (ICCF, e.g. Gaskell & Peterson 1987; Peterson et al. 1998, 2004), the discrete cross-correlation function (e.g. Edelson & Krolik 1988), regularized linear inversion (e.g. Krolik & Done 1995; Skielboe et al. 2015), the z-transformed cross-correlation function (ZDCF, e.g. Alexander 1997, 2013), the Fourier cross-spectrum (mainly for X-ray RM, e.g. Zhang 2002; Uttley et al. 2014; Epitropakis & Papadakis 2016), JAVELIN (e.g. Zu, Kochanek & Peterson 2011; Zu et al. 2013), and CREAM (e.g. Starkey, Horne & Villforth 2016). There have been many comparisons of these methods (e.g. Koen 1994; Kovačević et al. 2014; King et al. 2015; I-Hsiu Li et al. 2019). Here we focus on the effects of systematic errors for the two most commonly used algorithms, the ICCF method and JAVELIN.

The ICCF method linearly interpolates the light curves and calculates the CCF. Either the centroid $\tau_{\rm cent}$ or the peak $\tau_{\rm peak}$ of the CCF can be an estimate of the time lag. For the lag uncertainty, the algorithm randomly picks a subset of the epochs (with replacement) and/or randomizes the flux to create a number of independent realizations of the light curves. These realizations build up the cross-correlation centroid distribution (CCCD) and cross-correlation peak distribution (CCPD), and the widths of these distributions are used as the estimate of the lag uncertainty.

JAVELIN combines an approach originally introduced for gravitational lensing time delays (Press, Rybicki & Hewitt 1992a,b) with recent statistical models for quasar variability (e.g. Kelly, Bechtold & Siemiginowska 2009; Kozłowski et al. 2010; MacLeod et al. 2010; Zu et al. 2013). It models the AGN variability using a damped random walk (DRW) with a covariance function

$$S(\Delta t) = \sigma_{\rm DRW}^2 \exp(-|\Delta t/\tau_{\rm DRW}|) \quad (4)$$

where $\sigma_{\rm DRW}$ and $\tau_{\rm DRW}$ are the amplitude and characteristic time-scale, respectively. The DRW is a 'red noise' process at short time-scales with a power spectral density (PSD) slope of -2. The PSD flattens on time-scales much larger than $\tau_{\rm DRW}$. JAVELIN assumes that the line light curve is a shifted, smoothed and scaled version of the continuum light curve (i.e. equation 1), and fits for the time lag, the width of a top-hat transfer function and the scaling factor that best reproduces the light curves using a Markov Chain Monte Carlo (MCMC) algorithm. It estimates the lag uncertainty as the width of the posterior probability density distribution.

A number of studies have noted that ICCF and JAVELIN tend to derive different uncertainties, generally in the sense that the ICCF error estimates are larger (e.g. Fausnaugh et al. 2017; Grier et al. 2017; McHardy et al. 2018; Mudd et al. 2018; Czerny et al. 2019; Edelson et al. 2019). This has driven a range of speculations as to both the origin of the difference and as to which estimates are more reliable. Some considerations are the effect of incorrect light-curve error estimates, deviations of quasar variability from the DRW model and choices of the transfer function (a top hat by default in JAVELIN).

Correct lag uncertainty estimates are critical to the RM method. For example, lag uncertainty estimates directly affect the estimates of the intrinsic scatter in the scaling relation between the BLR size and the continuum luminosity (e.g. Kaspi et al. 2000; Bentz et al. 2013), which is widely used in single-epoch black hole mass estimates. Correct continuum lag uncertainties are important in constraining the accretion models and understanding the apparent discrepancy between the thin disc model and some observations (e.g. Shappee et al. 2014; Fausnaugh et al. 2016; Jiang et al. 2017). Therefore, a systematic study of these issues for the lag uncertainty estimates is necessary.

In this paper, we use observationally constrained simulated light curves to probe the effect of a broad range of systematic errors on the JAVELIN and ICCF methods. We focus on high-cadence light curves and do not consider sampling strategies or gaps due to weather, diurnal cycle, etc., as these have been examined in detail in previous studies (e.g. Horne et al. 2004; King et al. 2015; Shen et al. 2015; Yu et al. 2019; I-Hsiu Li et al. 2019). The structure of the paper is as follows. Section 2 describes the observations used to build the simulated light curves and the simulation methodology. In Section 3, we discuss the JAVELIN and ICCF results for all the different model configurations. We summarize our findings in Section 4.

2 METHODOLOGY

We base most of our simulations on the observed continuum light curves of four AGNs: NGC 5548, NGC 4151, NGC 4593, and Mrk 509. We show these observed light curves in Fig. 1. For NGC 5548, we adopt the 1367Å light curve from the *Hubble Space Telescope* (*HST*) as part of the AGN Space Telescope and Optical RM (AGN STORM) Project (De Rosa et al. 2015). HST monitored NGC 5548 with the Cosmic Origins Spectrograph from 2014 February 17 to July 22. The light curve includes 171 epochs with a typical cadence of about one day. We use the *Swift UVW2*-band light curves for the other three AGNs. *Swift* monitored NGC 4151 in 2016 from February 20 to April 29, yielding a light curve that consists of 319 visits with nearly five visits per day (Edelson et al. 2017). The light curve of NGC 4593 contains 148 epochs with a cadence of about 96 min from July 13 to 18 in 2016 and a cadence of about 192 min in the following 16.2 d (McHardy et al. 2018). The observations of Mrk 509 span from March 17 to December 15 in 2017 with 257 epochs separated by about one day (Edelson et al. 2019). We also carry out several tests using DRW light curves unconstrained by these observed light curves or using the *Kepler* light curve of Zw 229−15 (Edelson et al. 2014) for the simulated continuum.

We create simulated continuum light curves constrained by the observed light curves following the formalism of Zu et al. (2011) from Rybicki & Press (1992) based on theories of interpolation and prediction with a Gaussian process (e.g. Lewis & Odell 1971; Rao 1973; O'Hagan 1978). Let vector $\boldsymbol{y} = (y_1, y_2 \ldots y_{N_p})$ represent the light curve with N_p data points. The light curve $\boldsymbol{y} = \boldsymbol{s} + \boldsymbol{n} + \mathbf{L}\boldsymbol{q}$ is

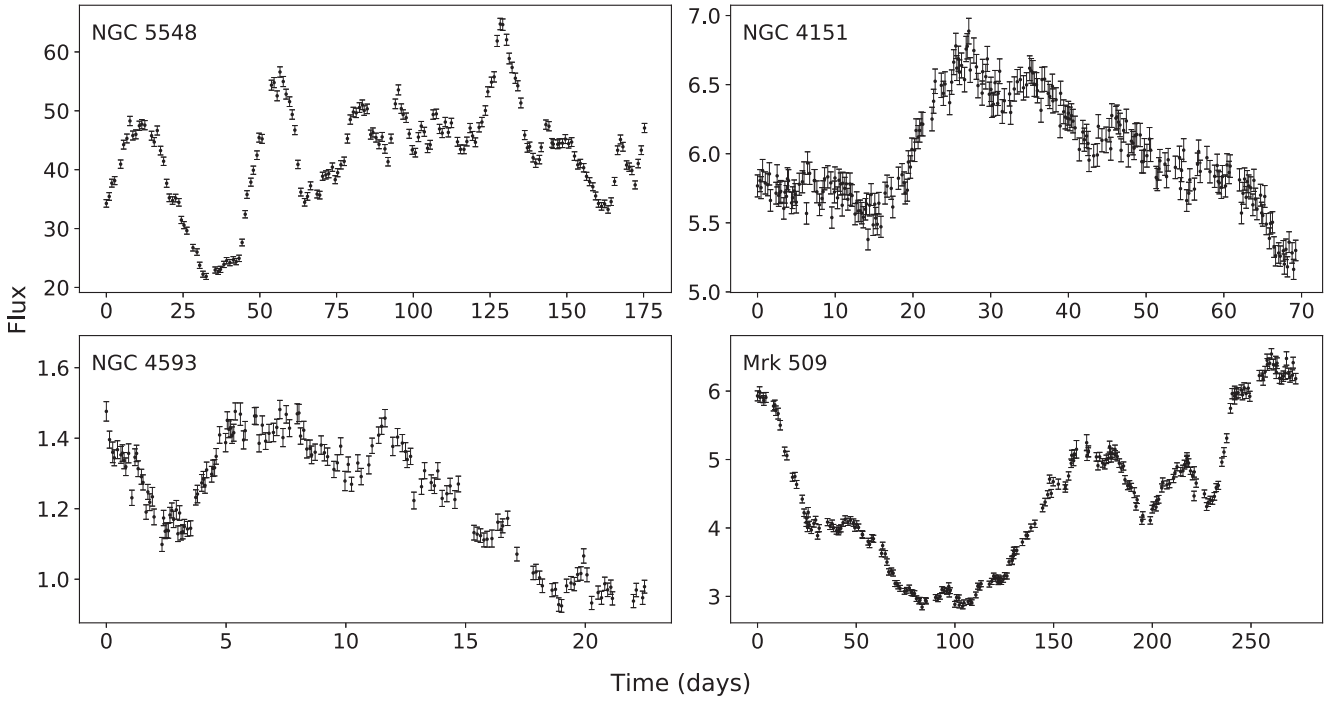

Figure 1. The *HST* 1367Å light curves of NGC 5548 (upper left), the *Swift UVW2*-band light curves of NGC 4151 (upper right), NGC 4593 (bottom left), and Mrk 509 (bottom right) used in our experiments.

a combination of the intrinsic signal $\boldsymbol{s}$, the noise $\boldsymbol{n}$, and a general trend $\mathbf{L}\boldsymbol{q}$. If the systematic trend is a constant background, $\mathbf{L}$ is a $N_{\rm p} \times 1$ matrix with all elements equal to one, and $\boldsymbol{q}$ is the best-fitting constant flux. While we only use a constant background, the linear parameters can also be used as a method to detrend the light curve as a polynomial ($a_0 + a_1 t + a_2 t^2$, etc.) or any other linear combination of functions. We define the signal covariance matrix $\mathbf{S} = \langle \mathbf{ss} \rangle$ and the noise covariance matrix $\mathbf{N} = \langle \mathbf{nn} \rangle$. The signal covariance matrix $\mathbf{S}$ depends on the assumed stochastic process for the quasar variability. If the noise is uncorrelated, the noise covariance matrix $\mathbf{N}$ is diagonal, and the diagonal elements are $N_{\rm ii} = \sigma_{\rm i}^2$, where $\sigma_{\rm i}$ is the measurement error for the ith epoch.

Rybicki & Press (1992) showed that for a given observed light curve $\boldsymbol{y}$, a signal covariance matrix $\mathbf{S}$ specified by the assumed stochastic process and a noise covariance matrix $\mathbf{N}$, the least-squares estimate of the mean of light curves consistent with the data is

$$\hat{\boldsymbol{s}} = \mathbf{S}\mathbf{C}^{-1}(\boldsymbol{y} - \mathbf{L}\hat{\boldsymbol{q}}) \tag{5}$$

and the best-fitting linear coefficients are

$$\hat{\boldsymbol{q}} = \mathbf{C}_{\rm q}\mathbf{L}^T\mathbf{C}^{-1}\boldsymbol{y} \tag{6}$$

where $\mathbf{C} = \mathbf{S} + \mathbf{N}$ and $\mathbf{C}_q = (\mathbf{L}^T\mathbf{C}^{-1}\mathbf{L})^{-1}$. The dispersion of the light curves around the mean is

$$\langle \Delta \boldsymbol{s}^2 \rangle = \mathbf{S} - \mathbf{S}^T\mathbf{C}_\perp\mathbf{S} \tag{7}$$

where $\mathbf{C}_\perp^{-1} = \mathbf{C}^{-1} - \mathbf{C}^{-1}\mathbf{L}\mathbf{C}_{\rm q}\mathbf{L}^T\mathbf{C}^{-1}$. Simulated light curves constrained by an observed light curve can also be constructed. The matrices $\mathbf{S}$ and $\mathbf{N}$ are given entries for the epochs both with and without data, while the noise is set to infinity (i.e. the corresponding entry in $\mathbf{N}^{-1}$ is zero) for the epochs without data. The model $\hat{\boldsymbol{s}}$ is constructed as before, but we then add a random component $\boldsymbol{u}$ with the covariance matrix

$$\mathbf{Q} = (\mathbf{S}^{-1} + \mathbf{N}^{-1})^{-1}. \tag{8}$$

To construct $\boldsymbol{u}$, we Cholesky decompose $\mathbf{Q} = \mathbf{M}^T\mathbf{M}$, and the random component is simply $\boldsymbol{u} = \mathbf{M}\boldsymbol{r}$, where $\boldsymbol{r}$ is a vector of independent Gaussian random deviates with zero mean and unit standard deviation (see Zu et al. 2011).

We fit the four observed light curves with JAVELIN. The time baselines of these light curves are too short to well constrain the time-scale $\tau_{\rm DRW}$, so we fix $\tau_{\rm DRW}$ to the estimated value from the empirical relation of MacLeod et al. (2010),

$$\begin{aligned}\log(\tau_{\rm DRW}) = {} & A + B\log(\lambda_{\rm RF}/4000\text{Å}) \\ & + C(M_i + 23) + D\log(M_{\rm BH}/10^9 {\rm M}_\odot)\end{aligned} \tag{9}$$

where $\lambda_{\rm RF}$ is the rest-frame wavelength of the observation, $M_{\rm i}$ is the i-band absolute magnitude, $M_{\rm BH}$ is the black hole mass, and $(A, B, C, D) = (2.4, 0.17, 0.03, 0.21)$. We use the best-fitting light curves and DRW parameters (when using the DRW model) to create simulated constrained light curves with 20 times the cadence of the observed light curves. We then resample the high-cadence simulated light curves to the cadence of the observed light curves through linear interpolations. Since the resampled light curves have much lower cadence than the original ones, the linear interpolation is adequate for the resampling. The exact value of $\tau_{\rm DRW}$ is not critical to the results. For example, even if we fix $\tau_{\rm DRW}$ in JAVELIN to 1/10 or 10 times the standard value, there is little effect on the lag estimates. Therefore, only a rough estimate of $\tau_{\rm DRW}$ is needed.

Given the mean noise of the observed light curve $\langle \sigma_{\rm i} \rangle$, we add Gaussian noise of dispersion $X_{\rm i}\langle \sigma_{\rm i} \rangle$ to the simulated light curves, where the coefficient $X_{\rm i}$ may depend on the epoch. For the analysis of the light curves, we say that the error is $Y_{\rm i}\langle \sigma_{\rm i} \rangle$, where this assigned uncertainty may differ from the actual noise (i.e. $X_{\rm i} \neq Y_{\rm i}$). We convolve the noiseless high-cadence continuum light curves with

Table 1. Simulation results for different sources and model configurations. Columns (1) and (2) give the configuration descriptions and the object names, respectively. Columns (3)–(5) give the median of $(t_{\rm fit} - t_0)$ from JAVELIN, CCCD and CCPD, respectively, where t_0 is the input lag and $t_{\rm fit}$ is the best-fitting lag from the algorithms. Columns (6)–(8) give the scatter $\sigma_{\rm obs}$ in $(t_{\rm fit} - t_0)$, defined as half the difference between the 16th and 84th percentile. Columns (9)–(11) give the mean error estimates $\sigma_{\rm est}$ from the algorithms. Columns (12)–(14) give the ratio $\eta = \sigma_{\rm est}/\sigma_{\rm obs}$, where $\eta > 1$ ($\eta < 1$) means that the lag uncertainties are over (under) estimated.

Configurations	Object name	Median $(t_{\rm fit} - t_0)$ (d)			$\sigma_{\rm obs}$ (d)			$\sigma_{\rm est}$ (d)			η		
		JAVELIN	CCCD	CCPD	JAVELIN	CCCD	CCPD	JAVELIN	CCCD	CCPD	JAVELIN	CCCD	CCPD
Baseline	NGC 5548	0.026	0.035	0.023	0.046	0.065	0.052	0.051	0.184	0.080	1.11	2.82	1.54
	NGC 4151	−0.002	−0.160	−0.038	0.102	0.168	0.099	0.114	0.257	0.259	1.12	1.53	2.60
	NGC 4593	0.000	−0.110	−0.013	0.034	0.043	0.045	0.036	0.077	0.077	1.06	1.81	1.71
	Mrk 509	0.017	−1.207	−0.055	0.095	0.199	0.089	0.104	0.388	0.159	1.09	1.95	1.80
Overestimated errors	NGC 5548	0.011	0.039	0.021	0.046	0.079	0.091	0.102	0.220	0.126	2.24	2.78	1.39
($Y_{\rm i} = 2$)	NGC 4151	0.041	−0.160	−0.034	0.119	0.157	0.114	0.295	0.410	0.492	2.48	2.61	4.32
	NGC 4593	−0.003	−0.132	−0.025	0.035	0.054	0.038	0.077	0.114	0.132	2.21	2.12	3.51
	Mrk 509	0.048	−1.303	−0.101	0.131	0.212	0.094	0.241	0.425	0.297	1.84	2.00	3.18
Underestimated errors	NGC 5548	0.014	0.021	0.024	0.064	0.077	0.052	0.037	0.172	0.068	0.59	2.24	1.31
($Y_{\rm i} = 0.5$)	NGC 4151	0.015	−0.174	−0.007	0.124	0.179	0.107	0.063	0.196	0.185	0.50	1.09	1.74
	NGC 4593	−0.001	−0.110	−0.014	0.043	0.051	0.039	0.030	0.065	0.057	0.70	1.26	1.46
	Mrk 509	0.013	−1.198	−0.019	0.119	0.194	0.087	0.053	0.372	0.126	0.44	1.92	1.45
Outliers	NGC 5548	0.027	0.033	0.026	0.054	0.081	0.064	0.051	0.184	0.084	0.96	2.28	1.32
($f_{\rm out} = 0.1$, $X_{\rm i} = 2$)	NGC 4151	0.007	−0.159	−0.017	0.127	0.166	0.130	0.108	0.266	0.286	0.85	1.60	2.19
	NGC 4593	−0.007	−0.124	−0.021	0.038	0.051	0.045	0.036	0.079	0.083	0.96	1.57	1.83
	Mrk 509	0.019	−1.267	−0.056	0.113	0.178	0.093	0.102	0.377	0.180	0.90	2.12	1.94
Outliers	NGC 5548	0.020	0.021	0.019	0.057	0.089	0.071	0.053	0.186	0.091	0.93	2.10	1.29
($f_{\rm out} = 0.2$, $X_{\rm i} = 2$)	NGC 4151	0.006	−0.186	−0.034	0.140	0.188	0.142	0.104	0.276	0.318	0.74	1.47	2.24
	NGC 4593	−0.004	−0.123	−0.021	0.046	0.052	0.048	0.037	0.082	0.088	0.80	1.56	1.86
	Mrk 509	0.026	−1.222	−0.054	0.117	0.192	0.119	0.099	0.386	0.184	0.84	2.01	1.54
Outliers	NGC 5548	0.017	0.028	0.031	0.094	0.109	0.087	0.053	0.192	0.098	0.57	1.77	1.13
($f_{\rm out} = 0.4$, $X_{\rm i} = 2$)	NGC 4151	0.013	−0.179	−0.017	0.187	0.216	0.179	0.094	0.298	0.358	0.50	1.38	2.00
	NGC 4593	0.003	−0.132	−0.022	0.056	0.071	0.064	0.039	0.086	0.100	0.69	1.21	1.55
	Mrk 509	0.030	−1.306	−0.085	0.191	0.256	0.146	0.100	0.393	0.213	0.52	1.53	1.46
Correlated errors	NGC 5548	0.024	0.021	0.023	0.045	0.058	0.051	0.051	0.182	0.080	1.14	3.15	1.57
(Same sign)	NGC 4151	0.004	−0.165	−0.032	0.091	0.127	0.100	0.113	0.252	0.262	1.25	1.98	2.63
	NGC 4593	−0.003	−0.115	−0.014	0.035	0.053	0.044	0.036	0.077	0.076	1.04	1.44	1.74
	Mrk 509	0.016	−1.189	−0.082	0.078	0.166	0.093	0.105	0.378	0.174	1.34	2.28	1.87
Correlated errors	NGC 5548	0.012	0.016	0.018	0.065	0.130	0.072	0.054	0.184	0.088	0.83	1.42	1.22
(Matern 3/2)	NGC 4151	−0.017	−0.257	−0.040	0.357	0.841	0.274	0.139	0.275	0.342	0.39	0.33	1.25
	NGC 4593	−0.003	−0.120	−0.018	0.045	0.065	0.055	0.036	0.078	0.080	0.82	1.20	1.47
	Mrk 509	0.051	−1.261	−0.093	0.175	0.388	0.166	0.106	0.367	0.177	0.60	0.95	1.07

a transfer function $\Psi(\tau)$ to create emission-line light curves. The transfer function $\Psi(\tau)$ has a small random mean lag t_0 between 2 and 4 d. This is simply to produce random offsets between the continuum and the line measurement epochs. While these small lag values were originally motivated by the small continuum lags, the particular value of the lag is unimportant for our simulations and the discussions are equally applicable to both line RM and continuum RM. We resample and add noise to the line light curves following the same process as for the continuum.

We focus on constrained realizations of actual AGN light curves to avoid any concern that the model light curves are somehow not representative of real AGNs. We did carry out a full set of experiments with unconstrained random realizations of light curves, and they produce similar results to those we describe below. There is one easily understood difference. We know that the constrained realizations will yield well-defined lags since they are based on light curves chosen for analysis and publication because they yielded lags. What we are concerned with here is whether those lags are accurate in the sense that the estimated lag and its uncertainty are consistent with the true lag.

Random light-curve realizations with the same cadence and noise levels are not guaranteed to yield lags because sometimes the light curve has no significant features (i.e. curvature, maxima, and minima) to allow a lag estimate. In such cases, any analysis will fail to give a significant lag measurement. As noted in the Introduction, the probability that a given sampling strategy will yield a light curve that will produce a lag has been well studied (e.g. Horne et al. 2004; King et al. 2015; Shen et al. 2015; Yu et al. 2019; I-Hsiu Li et al. 2019), which is why we do not make it a focus of our study.

3 RESULTS

We use JAVELIN and PYCCF (Sun, Grier & Peterson 2018), a PYTHON interface for the ICCF method, to measure the lags from the simulated light curves. For PYCCF, we create 8000 realizations with both flux randomization (FR) and random sub-sampling (RSS), and adopt the realizations with $r_{\rm peak} > 0.5$ to compute the ICCF lag uncertainties, where $r_{\rm peak}$ is the peak value of each CCF. Nearly all realizations pass the $r_{\rm peak}$ cut. For each CCF, we use the region with $r > 0.8 r_{\rm peak}$ to calculate the centroid and the peak. We compare the input lag t_0 and the output lags $t_{\rm fit}$ and characterize the results by four parameters: (1) the median of $(t_{\rm fit} - t_0)$; (2) the width $\sigma_{\rm obs}$ of the $(t_{\rm fit} - t_0)$ distribution, defined as half the difference between the 16th and 84th percentile; (3) the mean $\sigma_{\rm est}$ of the algorithm error estimates calculated as half the difference between the 16th and 84th percentile of the JAVELIN posterior probability distribution, CCCD or CCPD for each realization; and (4) the ratio $\eta = \sigma_{\rm est}/\sigma_{\rm obs}$ between the estimated uncertainty $\sigma_{\rm est}$ and the observed scatter $\sigma_{\rm obs}$, where $\sigma_{\rm obs}$ is an estimate of the 'true' uncertainty of the lag measurements and η indicates whether the algorithms overestimate ($\eta > 1$) or underestimate ($\eta < 1$) the lag uncertainties. We show these parameters for all the cases we consider in Tables 1–4. Fig. 2 illustrates the parameter ranges for the different cases we consider.

3.1 Baseline configuration

We first create simulated light curves that satisfy all the assumptions made by JAVELIN. We adopted DRW models with the parameters $(\sigma_{\rm DRW}, \tau_{\rm DRW}) = (17.38, 125)$, $(0.72, 136)$, $(0.49, 86)$, $(0.77, 146)$

Table 2. Same as Table 1, but for different model configurations.

Configurations	Object name	Median ($t_{\rm fit}-t_0$) (d)			$\sigma_{\rm obs}$ (d)			$\sigma_{\rm est}$ (d)			η		
		JAVELIN	CCCD	CCPD	JAVELIN	CCCD	CCPD	JAVELIN	CCCD	CCPD	JAVELIN	CCCD	CCPD
Isosceles-triangular $\Psi(\tau)$	NGC 5548	0.003	0.012	0.011	0.045	0.077	0.055	0.049	0.184	0.082	1.09	2.39	1.50
	NGC 4151	−0.080	−0.219	−0.101	0.087	0.159	0.089	0.108	0.258	0.240	1.24	1.62	2.69
	NGC 4593	0.036	−0.074	0.027	0.025	0.052	0.035	0.033	0.077	0.066	1.30	1.49	1.88
	Mrk 509	0.033	−1.176	−0.030	0.093	0.177	0.093	0.103	0.394	0.158	1.10	2.23	1.71
Forward-triangular $\Psi(\tau)$	NGC 5548	0.002	0.013	0.007	0.049	0.074	0.054	0.050	0.184	0.081	1.02	2.47	1.50
	NGC 4151	−0.079	−0.231	−0.096	0.094	0.167	0.095	0.111	0.255	0.249	1.18	1.52	2.63
	NGC 4593	0.032	−0.078	0.021	0.033	0.051	0.039	0.034	0.077	0.068	1.03	1.51	1.75
	Mrk 509	0.034	−1.228	−0.031	0.090	0.214	0.103	0.102	0.371	0.157	1.13	1.73	1.52
Long-tail $\Psi(\tau)$	NGC 5548	−0.110	−0.014	−0.175	0.075	0.076	0.142	0.077	0.177	0.142	1.03	2.32	1.00
	NGC 4151	−0.162	−0.307	−0.443	0.161	0.190	0.221	0.174	0.260	0.476	1.08	1.37	2.15
	NGC 4593	−0.323	−0.679	−0.694	0.105	0.131	0.137	0.098	0.124	0.210	0.94	0.94	1.53
	Mrk 509	−0.040	−0.248	−0.109	0.133	0.190	0.149	0.137	0.545	0.264	1.03	2.87	1.77
Double-exponential $\Psi(\tau)$	NGC 5548	−0.136	−0.016	−0.140	0.060	0.067	0.110	0.069	0.178	0.111	1.15	2.64	1.01
	NGC 4151	−0.200	−0.306	−0.350	0.143	0.157	0.171	0.159	0.256	0.413	1.11	1.63	2.41
	NGC 4593	−0.240	−0.441	−0.379	0.067	0.069	0.092	0.065	0.101	0.163	0.96	1.45	1.77
	Mrk 509	−0.043	−0.269	−0.093	0.118	0.178	0.105	0.131	0.547	0.233	1.11	3.07	2.21
Edge-on ring's $\Psi(\tau)$	NGC 5548	−0.048	−0.016	−0.019	0.059	0.068	0.163	0.081	0.178	0.177	1.36	2.64	1.09
	NGC 4151	−0.111	−0.348	−0.324	0.161	0.187	0.291	0.184	0.277	0.567	1.14	1.48	1.95
	NGC 4593	0.086	−1.014	−1.549	0.131	0.959	1.030	0.152	0.229	0.391	1.16	0.24	0.38
	Mrk 509	−0.025	−0.294	−0.077	0.107	0.177	0.149	0.142	0.543	0.289	1.32	3.07	1.93
'*Kepler*' process ($\tau_{\rm c}=2$ d)	NGC 5548	0.002	0.035	0.005	0.043	0.069	0.051	0.055	0.175	0.084	1.28	2.55	1.65
	NGC 4151	−0.011	−0.163	−0.034	0.105	0.165	0.125	0.128	0.251	0.311	1.21	1.52	2.48
	NGC 4593	−0.002	−0.113	−0.014	0.029	0.046	0.040	0.038	0.074	0.077	1.29	1.61	1.92
	Mrk 509	0.005	−1.210	−0.094	0.102	0.207	0.096	0.115	0.387	0.179	1.12	1.87	1.86
'*Kepler*' process ($\tau_{\rm c}=8$ d)	NGC 5548	−0.003	0.029	0.008	0.040	0.071	0.056	0.057	0.172	0.086	1.44	2.43	1.54
	NGC 4151	0.007	−0.128	−0.024	0.122	0.168	0.128	0.137	0.246	0.341	1.12	1.47	2.66
	NGC 4593	0.001	−0.114	−0.006	0.033	0.054	0.042	0.038	0.075	0.079	1.18	1.39	1.88
	Mrk 509	0.018	−1.173	−0.067	0.106	0.165	0.102	0.124	0.374	0.187	1.17	2.26	1.84
'*Kepler*' process ($\tau_{\rm c}=30$ d)	NGC 5548	0.002	0.041	0.011	0.048	0.069	0.064	0.058	0.170	0.081	1.19	2.47	1.27
	NGC 4151	0.016	−0.174	−0.037	0.121	0.165	0.137	0.144	0.247	0.367	1.19	1.50	2.69
	NGC 4593	0.002	−0.111	−0.009	0.035	0.045	0.044	0.038	0.075	0.080	1.10	1.66	1.81
	Mrk 509	0.030	−1.204	−0.058	0.099	0.132	0.081	0.127	0.366	0.188	1.29	2.77	2.33

Table 3. Simulation results from varying the backgrounds of the line light curves. Column (2) gives the random seed used to generate the background variation. The notation 'random' means we used a different random seed for each realization. Column (3) gives the standard deviation $\sigma_{\rm bkg}$ of the background variation. Other columns have the same meaning as Table 1.

Object name	Random seed	$\sigma_{\rm bkg}$	Median ($t_{\rm fit}-t_0$) (d)			$\sigma_{\rm obs}$ (d)			$\sigma_{\rm est}$ (d)			η		
			JAVELIN	CCCD	CCPD	JAVELIN	CCCD	CCPD	JAVELIN	CCCD	CCPD	JAVELIN	CCCD	CCPD
NGC 5548	20	3.430	0.206	0.530	0.250	0.123	0.075	0.078	0.127	0.209	0.136	1.04	2.78	1.75
	20	6.002	0.430	0.867	0.401	0.249	0.096	0.139	0.239	0.264	0.211	0.96	2.74	1.51
	30	3.430	0.030	0.189	0.081	0.130	0.071	0.057	0.140	0.221	0.127	1.07	3.12	2.24
	30	6.002	−0.067	0.335	0.137	0.215	0.092	0.082	0.232	0.274	0.195	1.08	2.98	2.38
	random	3.430	0.019	0.066	0.057	0.179	0.375	0.166	0.136	0.212	0.129	0.76	0.56	0.78
	random	6.002	−0.063	0.050	0.042	0.330	0.683	0.293	0.231	0.265	0.196	0.70	0.39	0.67
NGC 4151	40	0.150	0.929	1.121	0.520	0.293	0.212	0.235	0.167	0.263	0.420	0.57	1.24	1.79
	40	0.262	1.877	1.909	1.283	0.330	0.267	0.363	0.170	0.284	0.586	0.52	1.07	1.61
	50	0.150	0.074	0.556	0.059	0.152	0.232	0.140	0.118	0.315	0.343	0.78	1.36	2.46
	50	0.262	0.167	1.332	0.082	0.430	0.660	0.275	0.447	0.674	0.571	1.04	1.02	2.08
	random	0.150	0.139	0.093	0.034	0.775	1.575	0.628	0.151	0.306	0.429	0.19	0.19	0.68
	random	0.262	−0.077	−0.393	−0.134	2.134	3.305	1.857	0.984	0.502	0.704	0.46	0.15	0.38
NGC 4593	60	0.064	−5.631	−0.298	−0.060	3.351	0.099	0.054	3.728	0.108	0.109	1.11	1.09	2.03
	60	0.111	−5.940	−6.012	−6.058	0.557	1.447	0.690	3.321	0.914	1.063	5.97	0.63	1.54
	70	0.064	0.100	0.157	0.106	0.109	0.058	0.065	6.424	0.861	0.891	58.89	14.87	13.79
	70	0.111	0.101	−16.176	−16.244	3.458	8.607	8.586	7.823	3.273	3.343	2.26	0.38	0.39
	Random	0.064	−0.046	−0.085	−0.014	1.307	0.295	0.122	5.151	0.393	0.404	3.94	1.33	3.32
	Random	0.111	−0.826	−0.848	−0.323	3.177	7.787	7.906	5.034	1.357	1.409	1.58	0.17	0.18
Mrk 509	80	0.417	2.257	6.766	2.159	0.444	0.340	0.264	0.305	0.842	0.634	0.69	2.48	2.40
	80	0.729	3.597	21.705	17.775	0.973	0.516	11.641	0.689	1.023	13.166	0.71	1.98	1.13
	90	0.417	−3.480	−4.502	−1.037	0.765	0.364	0.350	0.605	0.951	0.876	0.79	2.61	2.50
	90	0.729	−7.618	−8.109	−6.199	1.941	0.250	0.543	1.390	0.888	2.170	0.72	3.55	3.99
	Random	0.417	0.388	−0.563	−0.027	2.545	4.658	1.850	0.377	0.727	0.556	0.15	0.16	0.30
	Random	0.729	−0.262	−0.395	0.029	3.944	9.468	3.999	0.800	1.055	1.255	0.20	0.11	0.31

for NGC 5548, NGC 4151, NGC 4593, and Mrk 509, respectively, where $\tau_{\rm DRW}$ is in units of days and $\sigma_{\rm DRW}$ is in the same flux units as the observed light curves. We created 200 realizations of the simulated continuum for each object. For each realization, we construct the line light curves by convolving the simulated continuum with a normalized top-hat transfer function with a width of 0.6 d and a random lag between 2 and 4 d. The particular value of the lag is unimportant here. We use some spread so that the alignment of the continuum and the line epochs varies. We assume Gaussian uncorrelated and correctly estimated noise like that in the observations (i.e. $X_{\rm i}\equiv Y_{\rm i}\equiv 1$). We then estimated the lags for all 800 light curves with both JAVELIN and ICCF. Several JAVELIN lag distributions for NGC 4593 show a weak secondary peak at ~ -10 d due to aliasing. Since this effect is well understood, we only consider the lag

Table 4. Results from simulated light curves based on the *Kepler* light curves of Zw 229−15. The *Kepler* light curves are sampled at the cadence of the *Swift* light curves of either NGC 4151 or NGC 4593. Columns (2) and (3) give the start and end time of the time intervals where we sample the *Kepler* light curve, respectively. Other columns have the same meaning as Table 1.

Cadence	Start time	End time	Median ($t_{\rm fit}-t_0$) (d)			$\sigma_{\rm obs}$ (d)			$\sigma_{\rm est}$ (d)			η		
	(HJD − 2400000)	(HJD − 2400000)	JAVELIN	CCCD	CCPD	JAVELIN	CCCD	CCPD	JAVELIN	CCCD	CCPD	JAVELIN	CCCD	CCPD
NGC 4151	55641.515	55710.915	−0.000	−0.038	−0.064	0.134	0.296	0.174	0.182	0.514	0.440	1.36	1.74	2.53
Cadence	56321.668	56391.068	0.019	0.051	0.021	0.105	0.125	0.137	0.123	0.204	0.314	1.17	1.64	2.30
	55757.235	55826.635	0.030	−0.719	−0.037	0.187	0.541	0.220	0.208	0.889	0.535	1.11	1.64	2.43
	56134.419	56203.819	−0.000	0.084	0.005	0.057	0.098	0.072	0.069	0.134	0.163	1.21	1.37	2.26
NGC 4593	55400.383	55423.083	0.009	−0.445	−0.018	0.072	0.102	0.081	0.083	0.205	0.193	1.14	2.02	2.39
Cadence	55871.416	55894.116	0.015	−0.277	−0.017	0.092	0.393	0.111	0.112	0.448	0.247	1.22	1.14	2.23
	56210.391	56233.091	0.065	−0.616	−0.108	0.093	0.082	0.113	0.106	0.175	0.242	1.14	2.14	2.15
	56277.349	56300.049	0.019	−0.230	−0.055	0.068	0.081	0.084	0.076	0.128	0.175	1.12	1.58	2.08

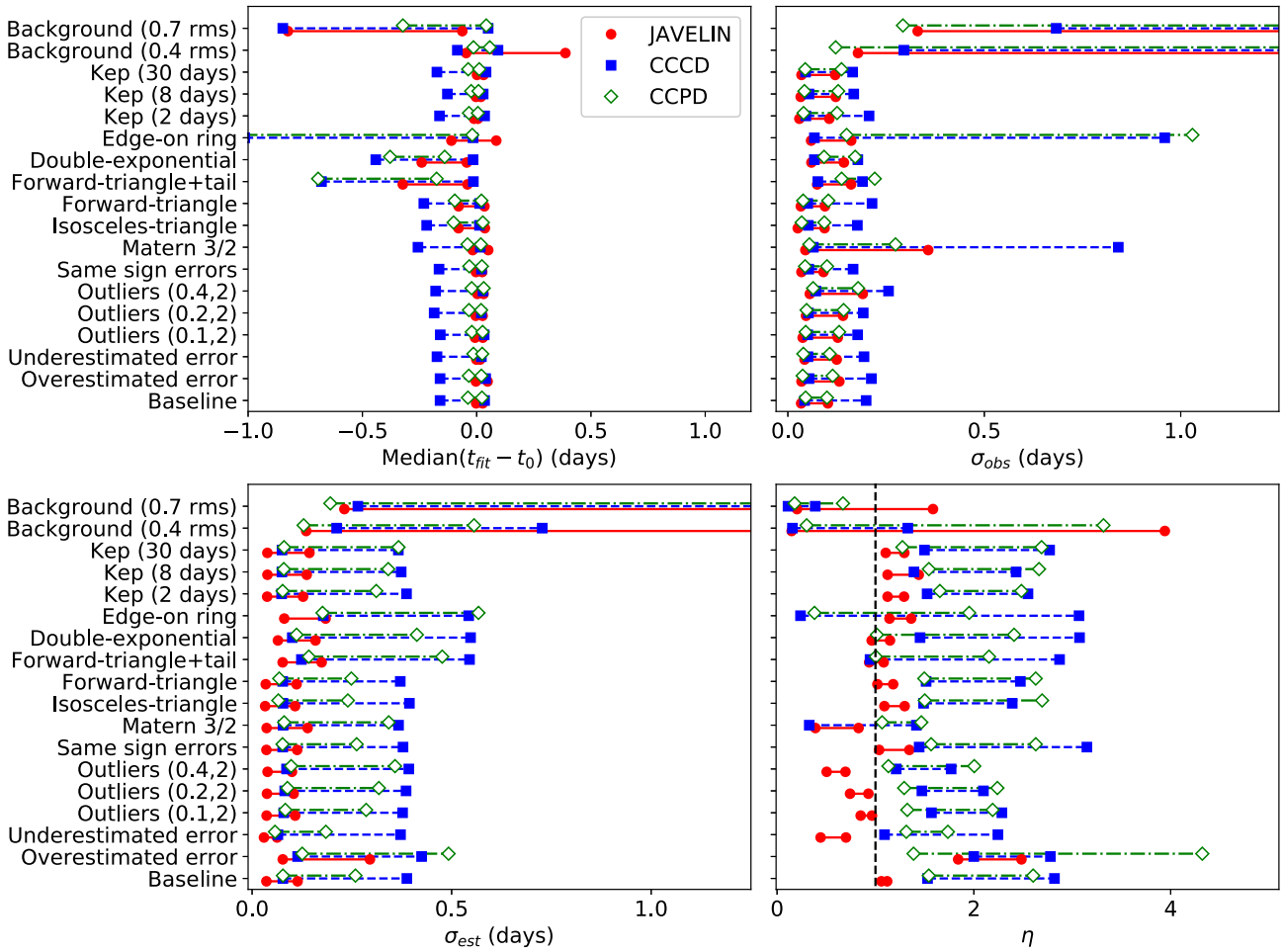

Figure 2. Comparison of the median ($t_{\rm fit}-t_0$) (upper left), $\sigma_{\rm obs}$ (upper right), $\sigma_{\rm est}$ (bottom left), and η (bottom right) estimates for the different cases. For the background variation cases, we only include the two with changing random seeds for each realization. For each case, the red circles, blue squares, and green empty diamonds are drawn at the maximum and the minimum parameter values for the four AGNs from JAVELIN, CCCD and CCPD, respectively. We add small shifts along the y-axis for each case to avoid overlapping between the points and lines. In the bottom right panel, the black dashed line is drawn at $\eta = 1$. The CCCD results for the median ($t_{\rm fit}-t_0$) in Mrk 509 deviate significantly from the input, so we did not include those results in the upper left panel of the figure for visibility.

distribution between −2 to 8 d for the uncertainty estimates in our analysis.

Fig. 3 shows the distribution of the difference ($t_{\rm fit}-t_0$) between the best-fitting lags $t_{\rm fit}$ and the input lags t_0 for NGC 5548. We only show the results for NGC 5548 as an example in the main body of the paper and include the results for the other three objects in the online journal. The median of the ($t_{\rm fit}-t_0$) distributions from all algorithms shows a slight offset from zero by around 0.02 d. This is likely a small artefact from the sampling or convolution process used to produce the simulated light curves. However, the 0.02 d offset is small compared the lag uncertainties and will not affect our conclusions. JAVELIN gives the smallest scatter $\sigma_{\rm obs}$ and the smallest error estimates $\sigma_{\rm est}$ among the three distributions, while CCCD gives the largest $\sigma_{\rm obs}$ and $\sigma_{\rm est}$. All algorithms overestimate the lag uncertainties with $\eta > 1$. The JAVELIN lag uncertainties are closest to the 'true' uncertainty with $\eta \approx 1.1$, while the CCCD and

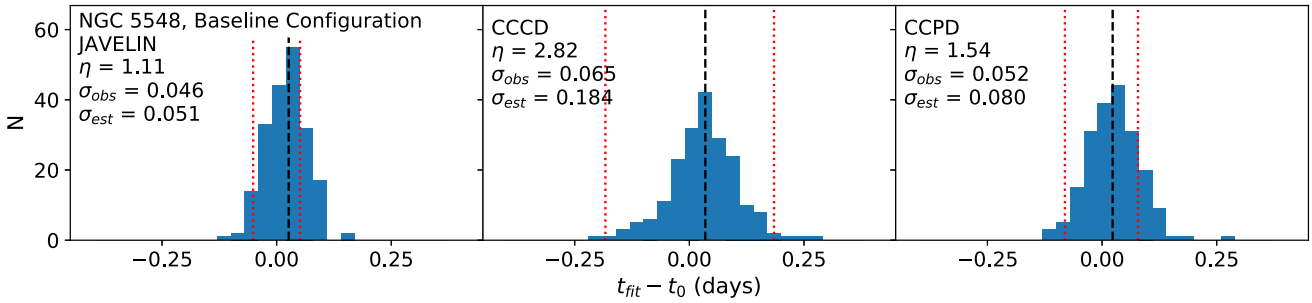

Figure 3. Distribution of the difference between the best-fitting lags $t_{\rm fit}$ and the input lags t_0 for NGC 5548. The black dashed lines are drawn at the median of the distribution ($t_{\rm fit} - t_0$), while the red dotted lines are drawn at the mean of the 1σ upper and lower limits estimated by the algorithms. The upper left corner of each panel reports the scatter $\sigma_{\rm obs}$ in the ($t_{\rm fit} - t_0$) distributions, the mean error estimates $\sigma_{\rm est}$ from the algorithms and the ratio $\eta = \sigma_{\rm est}/\sigma_{\rm obs}$. The left-hand, middle, and right-hand panels show the results from JAVELIN, CCCD, and CCPD, respectively.

CCPD methods overestimate the lag uncertainties with $\eta \approx 3$ and 1.5, respectively. We briefly explored restricting the ICCF method to only FR or only RSS rather than both. In most cases, this reduced the ratio η, but not in any systematic pattern, with FR sometimes having the greater effect and other times RSS. The ICCF method can underestimate the lag uncertainties (i.e. $\eta < 1$) with only FR or only RSS for some cases, while still overestimate the uncertainties (i.e. $\eta > 1$) for the others.

The other three objects generally show similar results to NGC 5548. The only poorly estimated lags, in the sense that the medians of ($t_{\rm fit} - t_0$) are more than $2\sigma_{\rm est}$, are the CCCD estimates for Mrk 509 with a median ($t_{\rm fit} - t_0$) = −1.2 d and $\sigma_{\rm est}$ = 0.38 d. JAVELIN consistently comes closest to correctly estimating the lag uncertainties with $\eta \approx 1.1$, while the CCCD and CCPD methods overestimate the uncertainties with η from 1.5 to 2.8. CCCD overestimates the lag uncertainty more severely than CCPD for some objects, while CCPD performs worse for the others. These differences between the uncertainty estimates from JAVELIN and ICCF are similar to those found in real RM campaigns (e.g. Fausnaugh et al. 2017; McHardy et al. 2018; Edelson et al. 2019).

We take these results as a 'baseline' for comparison with other cases. For the observed scatter $\sigma_{\rm obs}$, the estimated uncertainty $\sigma_{\rm est}$ and the ratio η, we say the parameter differs 'significantly' from the baseline if the parameter changes by more than 25 per cent. For the median ($t_{\rm fit} - t_0$), we do not say a change is significant as long as its absolute value is less than 0.1 d. We focus on the bulk behaviour in each case and do not discuss the behaviour of the individual objects in detail unless the results are driven by particular light-curve features.

3.2 Effect of input errors

In real RM campaigns, the uncertainties in the light curves may not be correctly estimated due to, for example, seeing-induced aperture effects on the spectra (e.g. Peterson et al. 1995). This will have consequences for the lag uncertainties. We consider several potential problems with the single-epoch error estimates.

3.2.1 Incorrect error estimates

We first artificially overestimate or underestimate the single-epoch uncertainties. The light curves are unchanged from the baseline configuration, but we either double ($Y_{\rm i} = 2$) or halve ($Y_{\rm i} = 0.5$) the uncertainties assigned to both the continuum and the line light curves, while keeping the actual noise unchanged ($X_{\rm i} = 1$). That is, we feed the algorithms with single-epoch errors that are two times larger or smaller than the noise that was actually added to the light curves.

We show the results in Fig. 4. Since the changes in this case have no effect on the 'shape' of the light curves, it is not surprising to find only small differences in the median ($t_{\rm fit} - t_0$) and the observed scatter $\sigma_{\rm obs}$ from the baseline case. When overestimating the uncertainties, the observed scatter $\sigma_{\rm obs}$ only varies slightly, except for the JAVELIN results for Mrk 509 and the CCPD results for NGC 5548. When underestimating the uncertainties, $\sigma_{\rm obs}$ consistently increases for JAVELIN, while it changes little for CCCD and CCPD. Both algorithms give larger lag uncertainties when overestimating the single-epoch uncertainties and smaller lag uncertainties while underestimating the single-epoch uncertainties. The ratio η roughly doubles/halves for JAVELIN when we double/halve the uncertainties, as expected from its strong assumption of Gaussian χ^2 uncertainties. On the other hand, the change in η for CCCD and CCPD is generally smaller, and η even slightly drops rather than increases when overestimating the uncertainties for NGC 5548. The ICCF method does not directly use the single-epoch uncertainties, which makes it less sensitive to incorrect estimates of the single-epoch uncertainties, albeit at the price of significantly overestimating the lag uncertainties if the error estimates are correct.

3.2.2 Outliers

Rather than having incorrect error estimates for all epochs, a light curve can contain 'outliers' that have intrinsically larger scatter than estimated. To simulate this, we select $f_{\rm out}N_{\rm p}$ points to be 'outliers' in both the continuum and the line light curves, where $N_{\rm p}$ is the total number of epochs and $f_{\rm out}$ is the outlier fraction. We increase the intrinsic scatter of each outlier to $X_{\rm i} = 2$ while keeping the intrinsic scatter of all other epochs at $X_{\rm i} = 1$. While we tried outliers with larger scatters (e.g. $X_{\rm i} = 8$), those outliers generally stand out from the light curves and can easily be identified and removed, so we do not consider those cases. We keep the assigned uncertainties unchanged for all epochs ($Y_{\rm i} = 1$) so that the algorithms assume there are no outliers, and we consider outlier fractions of $f_{\rm out} =$ 0.1, 0.2, 0.4.

Fig. 5 shows the results for NGC 5548. The medians of ($t_{\rm fit} - t_0$) show only small changes for both algorithms. The scatter $\sigma_{\rm obs}$ consistently increases with higher $f_{\rm out}$. The only exception is the CCCD results for NGC 4593, where the $\sigma_{\rm obs}$ for $f_{\rm out} = 0.1$ and $f_{\rm out} = 0.2$ are almost identical. The error estimate $\sigma_{\rm est}$ stays

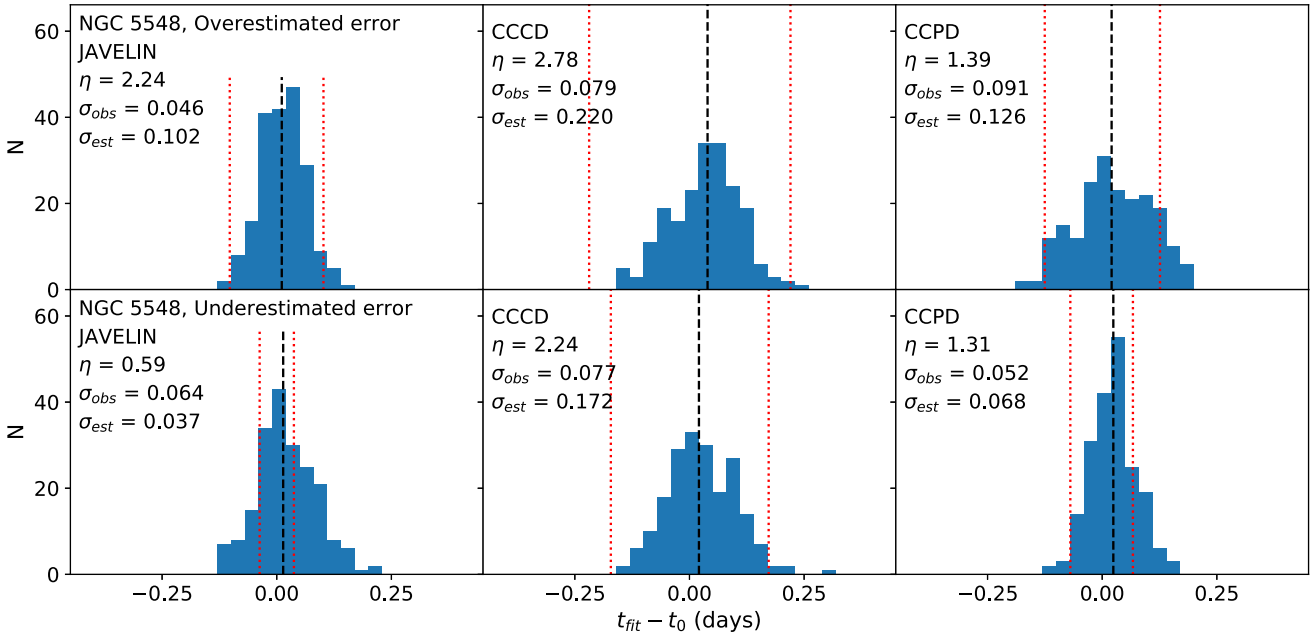

Figure 4. Same as Fig. 3, but for different configurations. The top row shows the results from overestimating the single-epoch errors, while the bottom row shows the results from underestimating the single-epoch errors.

nearly the same for JAVELIN, while it slightly increases at higher $f_{\rm out}$ for CCCD and CCPD. The ratio η consistently drops when $f_{\rm out}$ increases, except for the CCPD results for NGC 4593. Both algorithms are more likely to underestimate the lag uncertainties for large number of outliers, although this brings the ratio η for ICCF closer to unity from significantly overestimating the uncertainties in the baseline case. Like the previous cases, the ICCF results are less sensitive to the large outlier fraction, since the mistakes in single-epoch uncertainties affect JAVELIN directly but affect ICCF only indirectly.

3.2.3 *Correlated errors*

Correlations between the single-epoch errors may also affect the lag uncertainty estimates. One approach to simulating correlated errors is to make the noise added to the corresponding epochs of the continuum and the line light curves have the same sign. For example, if the noise added to an epoch of the continuum light curve is positive, then we require that the noise added to the line epoch for that date is also positive, although the amplitude can be different. In this case, the single-epoch errors between the continuum and the line light curves are correlated. This effect can be created in RM campaigns by flux calibration errors which bias the light-curve errors toward the same direction. The top row of Fig. 6 shows the results with this error correlation. The parameters for both JAVELIN and ICCF are generally consistent with the baseline configuration. The only exceptions are the CCCD results for NGC 4151 where the observed scatter $\sigma_{\rm obs}$ drops by about 25 per cent and the ratio η increases by about 30 per cent. The overall behaviour of the algorithms with such correlated error indicates that it has little impact on the lag measurements.

Another approach to adding correlated errors is to generate the noise with a Gaussian process. The method of adding noise in the baseline configuration is equivalent to a Gaussian process specified by a covariance matrix $N_{\rm ij} = \sigma_{\rm ns}^2\,\delta_{\rm ij}$, where $\sigma_{\rm ns} = X_{\rm i}\langle\sigma_{\rm i}\rangle$ and $\delta_{\rm ij}$ is the Kronecker delta function. We can make the noise correlated by adding non-zero off-diagonal terms

$$N_{\rm ij} = \sigma_{\rm ns}^2\,\delta_{\rm ij} + k(t_{\rm i}, t_{\rm j})\,. \tag{10}$$

Here, we model the correlated errors using a 3/2 power Matern (1960) kernel

$$k(t_{\rm i}, t_{\rm j}) = a^2\left(1 + \frac{\sqrt{3}|t_{\rm i} - t_{\rm j}|}{\tau_{\rm k}}\right)\exp\left(-\frac{\sqrt{3}|t_{\rm i} - t_{\rm j}|}{\tau_{\rm k}}\right). \tag{11}$$

Some studies on exoplanet transits (e.g. Johnson et al. 2015) use this kernel to model the correlated errors in transit light curves due to the variability of the host star. The parameter a characterizes the amplitude of the correlated errors and the parameter $\tau_{\rm k}$ describes the time-scale on which the errors are correlated. Here, we adopt $a = \sigma_{\rm ns}$ and $\tau_{\rm k} = 0.1\ \tau_{\rm DRW}$. We separately add the correlated noise generated through this method to the continuum and line light curves but then assume the standard diagonal noise matrix for the algorithms. Fig. 7 illustrates the difference between uncorrelated Gaussian and the correlated noise produced by the Matern 3/2 process. This error correlation model makes the noise tend to have the same sign on time-scales of $\tau_{\rm k}$.

We show the results for this correlated noise model in the bottom row of Fig. 6. For bothJAVELIN and ICCF, there is no significant change in the median of $(t_{\rm fit} - t_0)$. The estimated uncertainties $\sigma_{\rm est}$ increase by about 30 per cent for the NGC 4151 CCPD results. Otherwise the estimated uncertainties $\sigma_{\rm est}$ are generally consistent with the baseline. The observed scatter $\sigma_{\rm obs}$ generally becomes significantly larger, and the ratio η drops as a result. The change in $\sigma_{\rm obs}$ and η is most significant for the CCCD method and for NGC 4151. Unmodelled correlated noise appears to broaden the $(t_{\rm fit} - t_0)$ distribution and cause a non-negligible drop in η (i.e. it makes the algorithms more likely to underestimate the lag uncertainty). These temporally correlated errors have a bigger effect than the random outliers, because they are effectively a distortion in the light-curve shapes. This means they can act like a violation of the assumptions of equation (1) that the line light curve is a smoothed and delayed

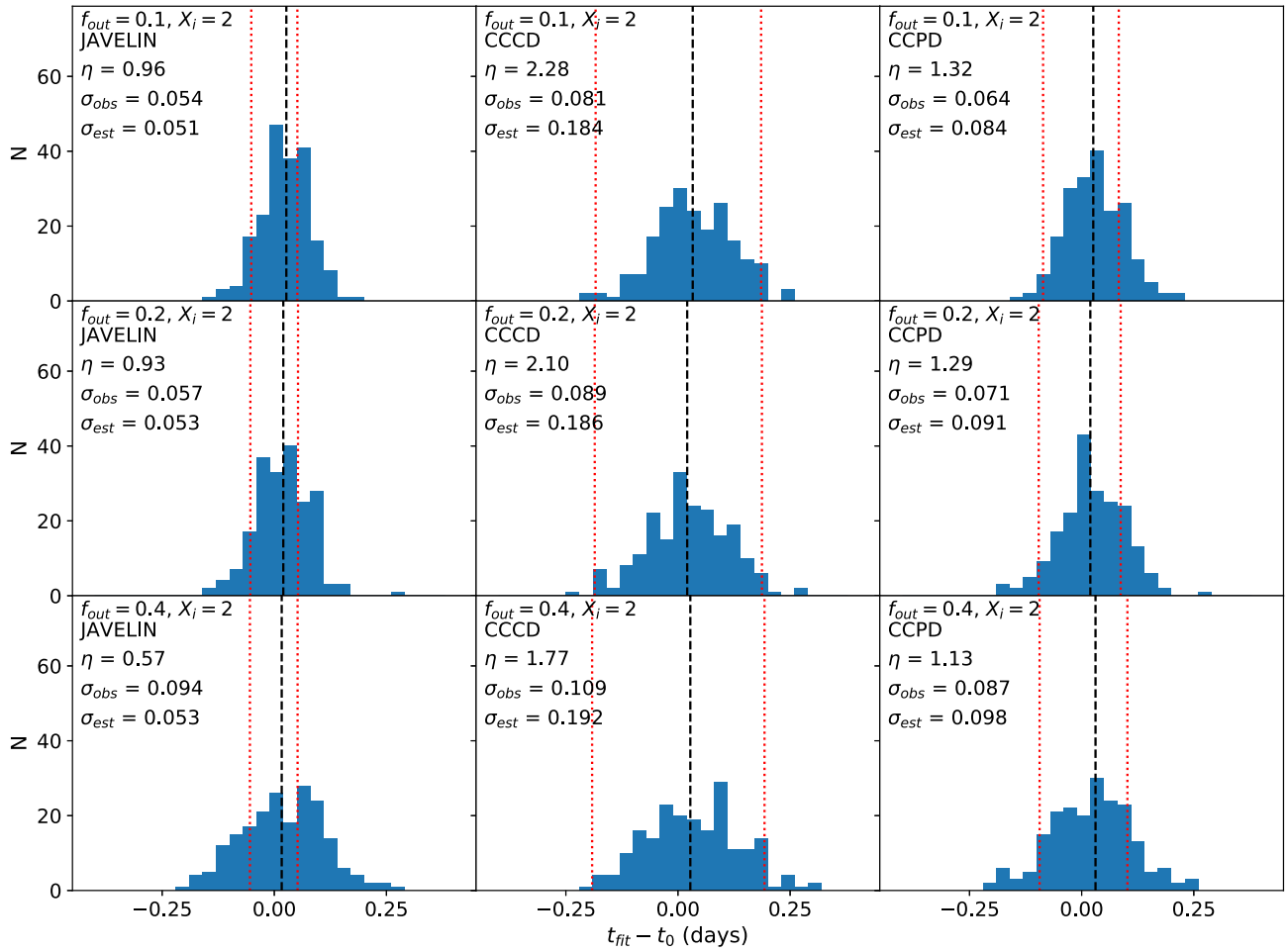

Figure 5. Same as Fig. 3, but for the light curves with outliers for NGC 5548. The left-hand, middle, and right-hand columns show the results from JAVELIN, CCCD, and CCPD, respectively. The top, middle, and bottom rows show the results from $f_{\rm out} = 0.1,\ 0.2,\ 0.4$, respectively, where $f_{\rm out}$ is the fraction of the outliers.

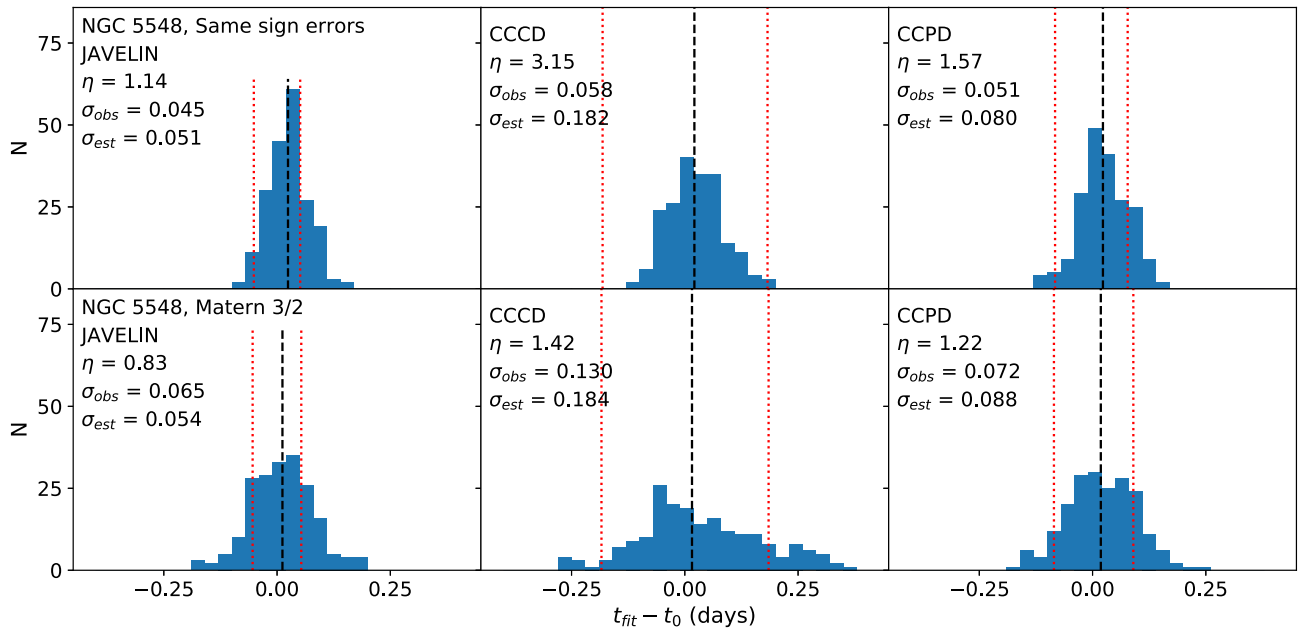

Figure 6. Same as Fig. 3, but for different configurations. The top row shows the results from making the errors of the continuum and the line light curves the same sign. The bottom row is for the case where we model the correlated errors with the Matern 3/2 model.

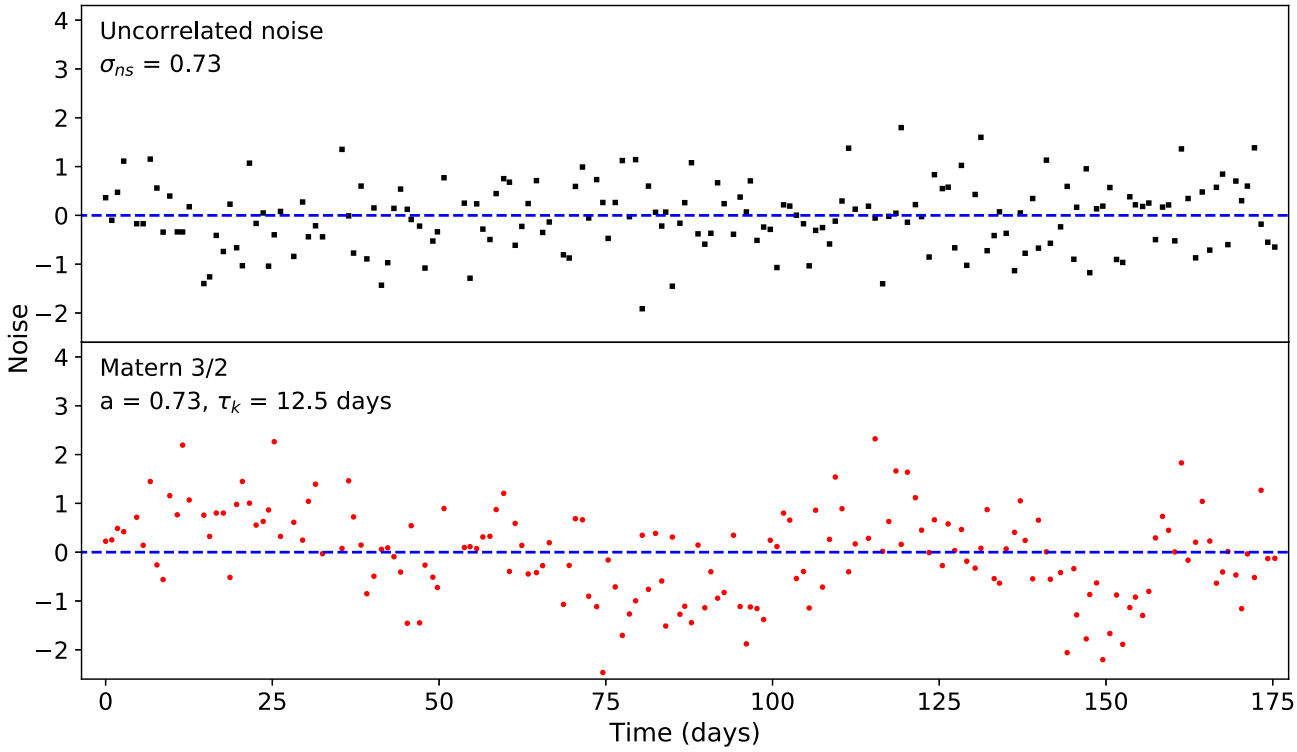

Figure 7. Comparison of the noise added to the simulated continuum light curve for NGC 5548 based on uncorrelated Gaussian errors (upper panel) and correlated errors from the Matern 3/2 model (lower panel). The upper left corner of each panel shows the parameters of noise models (equations 10 and 11). The blue dashed lines are drawn where the added noise equals zero.

version of the continuum. We explore this further in Section 3.5 where we explicitly add additional variability to the light curves.

3.3 Effect of transfer functions

In reality, the transfer function $\Psi(\tau)$ is not the top-hat function that we have assumed so far and is used in JAVELIN. McHardy et al. (2018) obtained a transfer function consisting of a strong peak followed by a long tail between the X-ray, UV and optical bands in NGC 4593. Horne et al. (in prep) recovered the emission-line transfer functions in NGC 5548, which generally show peaks at short lags and minor bumps at longer lags. Previous examinations of changing the transfer functions (e.g. Rybicki & Kleyna 1994; Zu et al. 2013) have found little effect on lag estimates.

Here we use five transfer functions other than the top hat, including an isosceles triangle, a 'forward' triangle, a combination of two forward triangles to produce a narrow peak with a long tail, a combination of two exponentials and the transfer function of an edge-on ring. We set the width of the single triangular transfer functions to be the same as the width of the previous top-hat function and use the same mean lags as in the baseline configurations. For the combination of two triangles, we set the width of the second triangle to be 10 times the width of the top hat, so the function looks like a forward triangle followed by a long tail. The double-exponential transfer function has the analytic form

$$\Psi(t) = A(1 - \mathrm{e}^{-x})\mathrm{e}^{-y}\,, \tag{12}$$

where $x = (t - t_0)/w_1$ and $y = (t - t_0)/w_2$. We adopt w_1 equal to the top-hat width and $w_2 = 1.2$ d so that the function has similar width to the double-triangular transfer function. We unify the function with $A = (w_1 + w_2)/w_2^2 \approx 1.26$, and the time offset t_0 is determined given $w1$, $w2$, and the mean lag $\langle\tau\rangle$. The normalized transfer function of an edge-on ring has the analytic form

$$\Psi(t) = \frac{1/\pi}{\sqrt{t(2\langle\tau\rangle - t)}}\,, \tag{13}$$

where $\langle\tau\rangle$ is the mean lag. Fig. 8 shows examples of the four transfer functions which by construction all have a mean lag of 2 d. In making these comparisons, it is important to use the correct mean lags (equation 2) for the different transfer functions. While this is not crucial for the symmetric transfer functions, the mean lag for asymmetric transfer functions is not at the mid-point.

We show the results in Fig. 9. For the isosceles and forward triangles, the medians of the $(t_{\rm fit} - t_0)$ distribution remain close to zero. The scatter $\sigma_{\rm obs}$, the estimated uncertainty $\sigma_{\rm est}$ and the ratio η are generally consistent with the baseline configurations. For the forward triangle with a long tail and the double-exponential transfer function, the algorithms tend to systematically underestimate the lag in the sense that the median $(t_{\rm fit} - t_0)$ is negative, although the systematic shifts are small relative to the input lags. This is not surprising because by more heavily smoothing the light curve, it is more difficult to detect the tail than the peak, which will tend to give the narrow peak more weight and lead to the bias. The observed scatter $\sigma_{\rm obs}$ and the estimated uncertainty $\sigma_{\rm est}$ increase in general, especially for JAVELIN and CCPD, while η stays nearly unchanged except for the NGC 4593 and Mrk 509 CCCD results and the NGC 5548 CCPD results.

For the edge-on ring, the median $(t_{\rm fit} - t_0)$ of the NGC 4593 ICCF results deviates significantly from zero, while the others generally show similar behaviour to the baseline results. Both $\sigma_{\rm obs}$ and $\sigma_{\rm est}$ increase in most cases, especially for NGC 4593. The significantly larger $\sigma_{\rm obs}$ leads to small η for the NGC 4593 ICCF results,

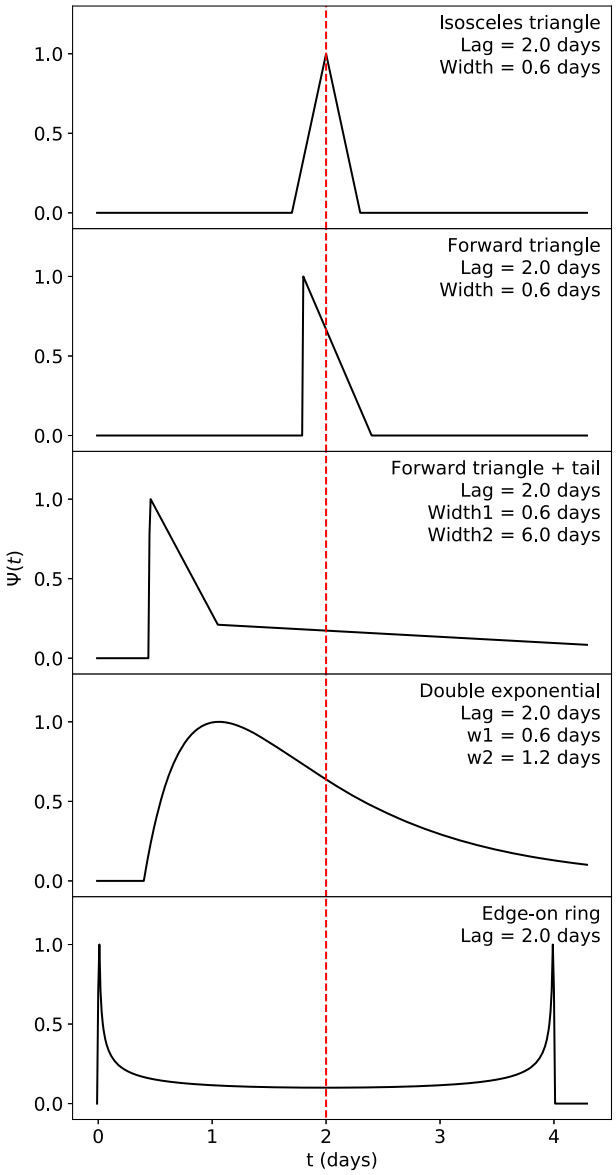

Figure 8. Examples of the isosceles-triangular transfer function (top), the forward-triangular transfer function, the triangular transfer function with a long tail, the double-exponential transfer function and the transfer function of an edge-on ring (bottom). The transfer function parameters are given in each panel. The transfer functions are normalized to have the same peak value for visibility. The red dashed line is drawn at 2 d, the mean lag of the transfer functions.

indicating that ICCF does not work well in this specific case. This is not surprising. NGC 4593 has the shortest observational baseline and the large temporal width of the edge-on ring transfer function leads to a significant smoothing of the light-curve variability. In general, the error ratio η does not change significantly for the JAVELIN and the other ICCF results. Overall, the form of the transfer function is not critical to the lag measurement for either algorithm.

The widths of the top-hat and the triangular transfer functions used above were small relative to the observational time baseline. We tried a top-hat transfer function with a width w that is roughly 10 per cent of the temporal length of the light curve. We adopt w = (17, 7, 3, 27) d for NGC 5548, NGC 4151, NGC 4593, and Mrk 509, respectively. This leads to much more smoothing of the line light curve relative to the continuum. We use a random lag between $w/2$ and $w/2 + 2$ d for each realization. The bottom row of Fig. 9 shows the results for NGC 5548. The median ($t_{\rm fit} - t_0$) shows larger deviation from zero relative to the baseline results for ICCF, while it does not change significantly for JAVELIN. The observed scatter $\sigma_{\rm obs}$ and the estimated uncertainty $\sigma_{\rm est}$ both increase, while the ratio η stays nearly unchanged. We also tried the forward-triangular transfer functions with these larger widths. We got similar results except for the systematic shift due to the more weighted peak than the tail as discussed above. However, the shift is only ∼3 per cent of the overall width of the transfer function. More strongly smoothing the light curve increases the uncertainties as expected, but the qualitative properties of the algorithms are unchanged. We expect this would hold if repeated for the other model transfer functions.

JAVELIN assumes a top-hat transfer function and fits for the top-hat width and scale in addition to the lag. While JAVELIN is generally able to recover the input lag, it usually cannot accurately recover the top-hat width. Essentially, the top-hat width and the scale factor between the line and continuum light curves are roughly degenerate when fitting typical data (see Zu et al. 2011). In order to probe whether the large uncertainties in these parameters affect the lag measurements, we fit the simulated light curves in the baseline configurations with the top-hat width fixed to twice/half the input value. Fig. 10 shows the results from NGC 5548. There is no significant change in the median ($t_{\rm fit} - t_0$), the observed scatter $\sigma_{\rm obs}$, the estimated uncertainty $\sigma_{\rm est}$ and the ratio η. We also tried fixing the scale to incorrect values and obtained similar results.

3.4 Effect of the stochastic process

Several studies of *Kepler* light curves found that AGN variability deviates from the DRW model and can have a steeper PSD on time-scales shorter than ∼ month (e.g. Mushotzky et al. 2011; Kasliwal et al. 2015; Smith et al. 2018). Zu et al. (2013) also saw weak evidence of this in Optical Gravitational Lensing Experiment (OGLE) light curves. We use two methods to explore the effects of the deviations from the DRW model, particularly at short time-scales.

3.4.1 Kepler covariance model

In the first test, we continue to use light curves constrained to resemble our four AGNs but generated using a different stochastic process. We use the '*Kepler*' process adopted by Yu et al. (2019), with the covariance function

$$S(\Delta t) = \sigma^2\,[(1+C)\exp(-|\Delta t/\tau_1|) - C\exp(-|\Delta t/\tau_2|)] \qquad (14)$$

where $C = \tau_2/(\tau_1 - \tau_2)$, σ is an amplitude equivalent to $\sigma_{\rm DRW}$, and τ_1 is a time-scale equivalent to $\tau_{\rm DRW}$ in the DRW model. We can vary $\tau_2 < \tau_1$ to produce a cut-off in the structure function at short time-scales. However, τ_2 is not an intuitive indicator of the cut-off time-scale, since the '*Kepler*' structure function starts to deviate from DRW at several times τ_2. We therefore define a cut-off time-scale $\tau_{\rm c}$ at which the '*Kepler*' structure function has 85 per cent the power of DRW. We adopt $\tau_{\rm c}$ = 2, 8, 30 d and numerically solve for τ_2 given each $\tau_{\rm c}$. Fig. 11 compares the DRW and the '*Kepler*' structure functions. This covariance function allows a cut-off at a wider range of time-scales than the 'Kepler-exponential' model from Zu et al. (2013) without the problem of a non-positive definite matrix.

We then create simulated light curves using the '*Kepler*' process with other parameters fixed to those in the baseline configuration.

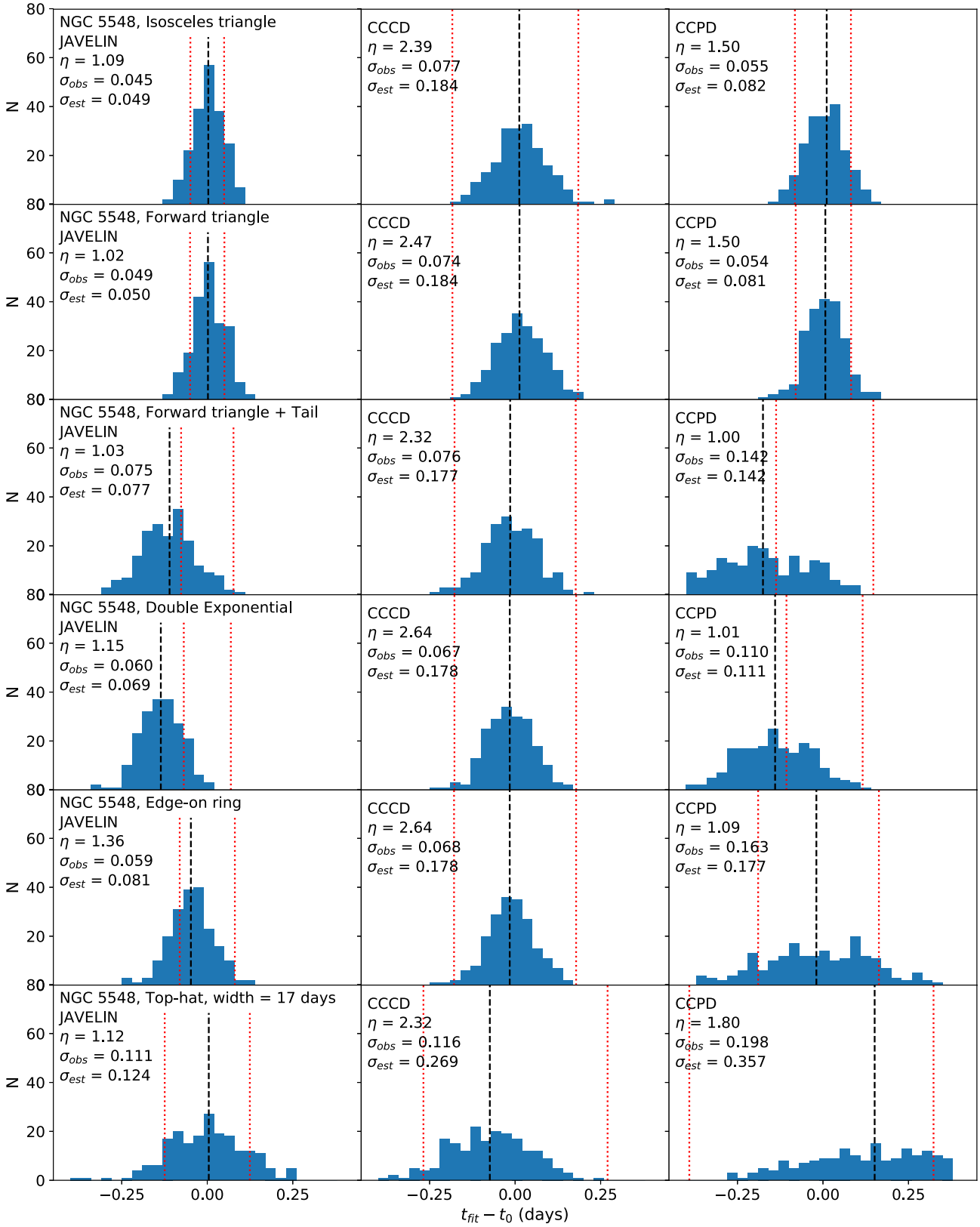

Figure 9. Same as Fig. 3, but for different transfer functions.

Fig. 12 compares a realization of the DRW and the '*Kepler*' process light curves for NGC 5548 with $\tau_c = 8$ d and using the same random seed so that the differences are only due to the change in the structure functions. The '*Kepler*' process light curve has less power at short time-scales and is therefore smoother than the DRW light curve. However, after we resample and add noise to the light curves, the differences are rather subtle.

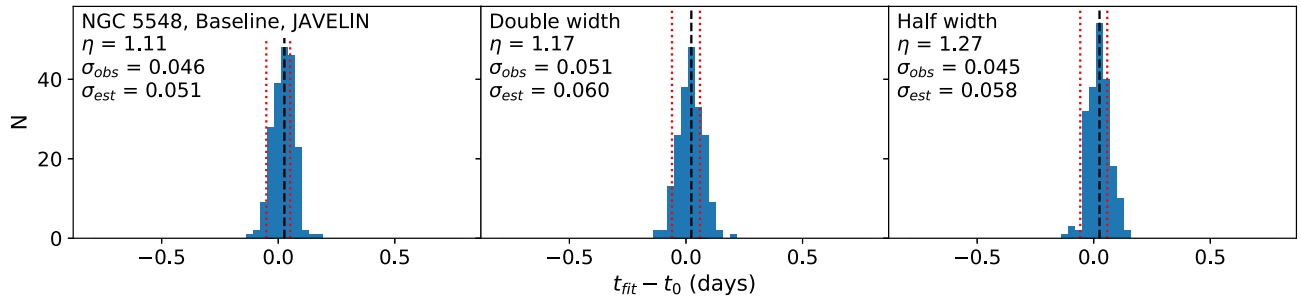

Figure 10. Same as Fig. 3, but for the JAVELIN results with fixed top-hat width. The left-hand panel shows the JAVELIN results for the baseline configurations (same as the first panel of Fig. 3). The middle and right-hand panels show theJAVELIN results with the top-hat width fixed to twice and half the input values, respectively.

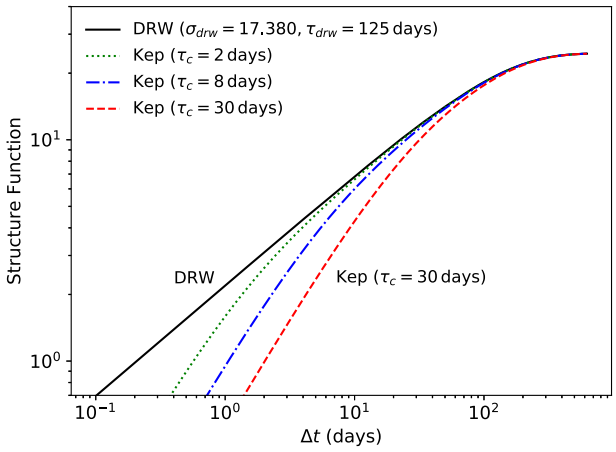

Figure 11. Structure functions of the DRW and the '*Kepler*' covariance models for NGC 5548. The blue solid line represents the DRW, while the red dashed, blue dashed–dotted, and green dotted lines represent the '*Kepler*' covariance model with τ_c = 2, 8, 30 d, respectively.

Fig. 13 shows the JAVELIN and ICCF results for the '*Kepler*' process light curves. In most cases there is no strong variation in the median ($t_{fit} - t_0$), the observed scatter σ_{obs}, the estimated uncertainty σ_{est} and the ratio η. The CCPD results for NGC 4151 give larger σ_{obs} and σ_{est} relative to the baseline, while the ratio η stays nearly the same. For τ_c = 8 d, the ratio η from JAVELIN for NGC 5548 increases by about 30 per cent due to a slight drop of σ_{obs} and a slight rise of σ_{est}. Overall, the deviations from the DRW model on short time-scales do not have a significant impact on the lag measurements.

3.4.2 *Observed Kepler light curve*

Our second test is to use the *Kepler* light curve of Zw 229−15 (Edelson et al. 2014) shown in the top panel of Fig. 14. We select four time intervals within the *Kepler* baseline that have the same length as the *Swift* observations of NGC 4151 or NGC 4593, where few epochs within these intervals lie in the gaps of the *Kepler* light curve. We do not use the observations of NGC 5548 or Mrk 509 because their time baselines are too long to fit into a single *Kepler* quarter. In each time interval, we resample the *Kepler* light curve to the cadence of the *Swift* observations and use it as the simulated continuum light curve. We assign uncertainties to the resampled epochs so that the ratio of the single-epoch uncertainty to the standard deviation of the light curve is the same as the *Swift* light curves. The simulated continuum light curve in each interval can be viewed as an independent 'realization' of the observed *Kepler* light curve. We then create 200 simulated line light curves for each of the four 'realizations' following the procedures in Section 2. The bottom panel of Fig. 14 shows an example of the *Kepler*-based simulated light curves. The light curve shows weaker variations on short time-scales than the DRW model.

Table 4 gives the JAVELIN and ICCF results for the four 'realizations' for these simulated light curves and Fig. 15 shows the results for NGC 4593. The median ($t_{fit} - t_0$) generally stays close to zero, except the CCCD results for NGC 4593 and one realization of NGC 4151. It is not meaningful to directly compare the observed scatter σ_{obs} and the estimated uncertainties σ_{est} to the baseline results since the light-curve shapes are different. However, the ratio η still indicates the correctness of the lag uncertainty estimates. In most cases, the ratio η does not change significantly relative to the baseline results. This again indicates that any deviation of the continuum from the DRW assumption has little effect on the lag measurements.

For some of the *Kepler* realizations, the CCCD results have an observed scatter σ_{obs} much larger than the other realizations. Most of these light curves show strong systematic trends, which can make it hard for the ICCF method to recover lags. If we detrend these light curves by fitting and subtracting a linear trend, CCCD generally shows better performance with smaller scatter σ_{obs} relative to the cases before detrending. The detrending also gives an η ratio closer to the other realizations, and none of the realizations produce significantly different η from the baseline results for the CCCD method after the detrending. We repeated this *Kepler* light-curve test with additional tens of 'realizations' for the NGC 4593 *Swift* cadence, and we got similar results except for the light curves where there is little variability after detrending and we do not expect a lag measurement.

3.5 Varying backgrounds

RM makes the strong assumption that the line light curve is a smoothed and shifted version of the observed continuum light curve with a constant background level. However, Horne et al. (in prep) found that this linear model fails for the observed light curves of NGC 5548, and they needed a time-dependent background $L_0(t)$ instead of the constant background level L_0 in equation (1) to obtain a good fit. This varying background may also explain the anomalous decoupling of the far-UV continuum and the broad-line variations found by Goad et al. (2016). The most significant feature of the $L_0(t)$ found by Horne et al. (in prep) is a drop from MJD 56740 to 56810

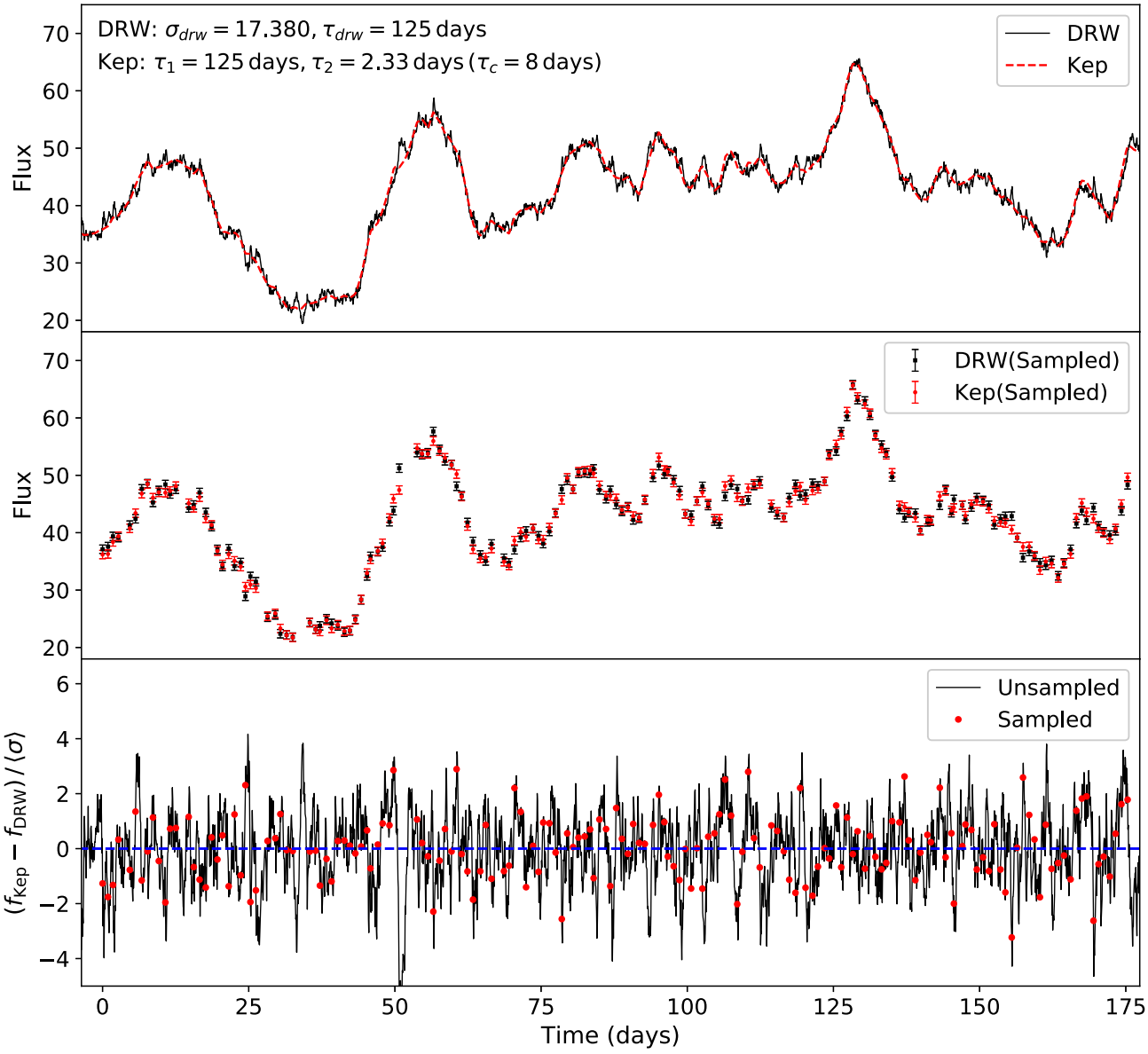

Figure 12. Comparison of the simulated continuum light curve for NGC 5548 based on the DRW and the '*Kepler*' process models. The top panel shows the high-cadence noiseless light curves. The black solid line is the DRW light curve, while the red dashed line is the '*Kepler*' process light curve. The middle panel shows the light curves as they would be observed by the AGN STORM campaign in both cadence and noise. The black squares and red circles are the DRW and the '*Kepler*' process light curves, respectively. The bottom panel shows the residual from subtracting the DRW and the '*Kepler*' process light curves divided by the mean light-curve errors. The black solid line and the red circles represent the residuals for the unsampled and sampled light curves, respectively.

followed by a more rapid rise back until MJD 56840. The origin of this variation is not well understood. It may appear because the observed continuum is not the relevant extreme UV ionizing continuum, or due to the change of the line-of-sight covering factor of the obscurers absorbing the soft X-rays (e.g. Mathur et al. 2017; Dehghanian et al. 2018; Goad et al. 2019; Kriss et al. 2019).

We model this sort of behaviour by a set of Legendre polynomials. For a line light curve within time range $t_0 < t < t_0 + t_m$ (i.e. the original light curve spans 0 to t_m but we then add a lag of t_0), we model the background as

$$L_0(t) = \sum_{i=1}^{N} a_i P_i(x)\,, \text{ where } x = 1 + 2(t - t_0 - t_m)/t_m \qquad (15)$$

and $P_i(x)$ is the ith order Legendre polynomial. We adopt a maximum order $N = 4$ and exclude the zeroth order so that $\langle L_0(t)\rangle = 0$. We choose the coefficients as

$$a_i = r_i \sigma_{bkg} \sqrt{\frac{2i+1}{N}} \qquad (16)$$

where i is the order of the Legendre polynomial, r_i is a Gaussian random variable with zero mean and unit dispersion, and σ_{bkg} is the desired standard deviation in $L_0(t)$. We choose this normalization so that each order contributes equally to σ_{bkg}. We then linearly detrend $L_0(t)$ using the starting and ending point of the background light curve to avoid adding a strong systematic trend that can affect lag measurements even when also present in the continuum. The resultant standard deviation of $L_0(t)$ may differ from σ_{bkg} due to

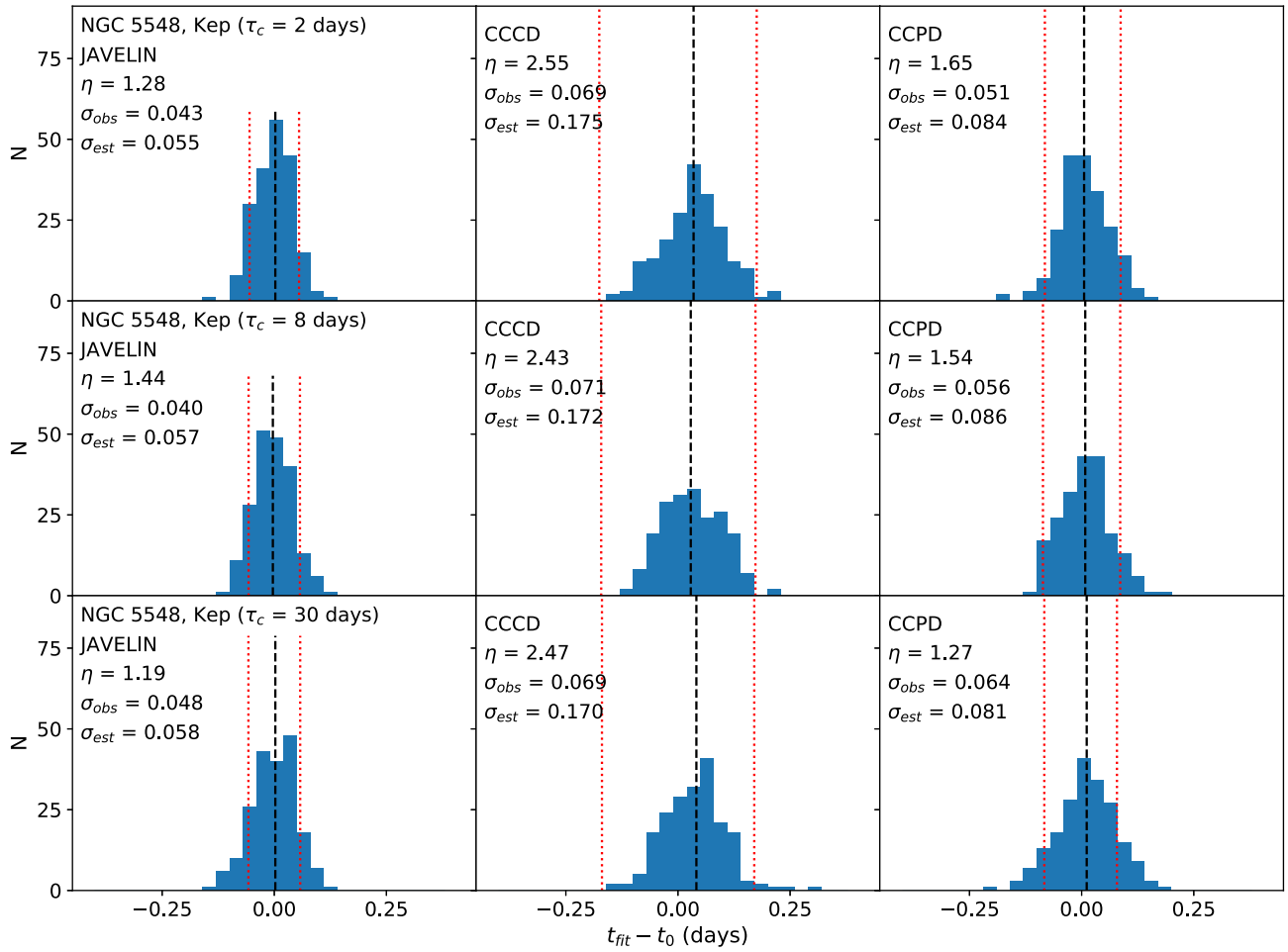

Figure 13. Same as Fig. 3, but for the '*Kepler*' covariance models.

the random variable and the linear detrending, so we rescale $L_0(t)$ so that its standard deviation equals $\sigma_{\rm bkg}$. These choices lead to distortions that resemble those found for NGC 5548 in Horne et al. (in prep).

We considered two cases. In the first set of models, we generate two random backgrounds for each source and held the random seeds fixed. Here, we expect to find a bias in the lag estimate. The observed scatter $\sigma_{\rm obs}$ can also increase, but the change would be less significant than the shift in the median $(t_{\rm fit} - t_0)$. In the second set of models, we randomly vary the backgrounds in each realization while holding the standard deviation $\sigma_{\rm bkg}$ fixed. This mimics repeated measurements of the same AGN, and here we expect the median of the $(t_{\rm fit} - t_0)$ distribution to be close to zero, but the dispersion $\sigma_{\rm obs}$ to be considerably larger due to the scatter in the individual estimates of the lag created by the varying backgrounds.

We first used two random seeds to generate the background light curve for each source. We set $\sigma_{\rm bkg}$ to 0.4 or 0.7 times the standard deviation of the observed light curve for each random seed. These ratios are typical of the background $L_0(t)$ used by Horne et al. (in prep). Fig. 16 shows an example of the line light curve after adding a varying background. The lags of these light curves are likely to deviate significantly from the input due to the deviation of the resampled line light curves (red points) from the high-cadence light curve (red solid line) with a constant background. We therefore consider lags outside of the −2 to 8 d range for the analysis here.

Table 3 includes the model parameters and the JAVELIN and ICCF results after adding the varying backgrounds. Fig. 17 shows the results for NGC 5548. In most cases, the median of $(t_{\rm fit} - t_0)$ deviates significantly from zero. These shifts are also 'visible' in the light curves. When the line light curve is rising, pulling the light curve down seems to move the light curve further right and leads to a larger lag. On the other hand, when the line light curve is declining, a drop in the light curve seems to move the light curve left and makes the lag smaller. The resultant median of $(t_{\rm fit} - t_0)$ is a balance between these two features. The scatter $\sigma_{\rm obs}$ and the estimated uncertainty $\sigma_{\rm est}$ increase significantly relative to the baseline. The ratio η stays nearly the same for the NGC 5548 JAVELIN results, but otherwise does not show a consistent pattern. Both algorithms are likely to give incorrect lags and uncertainties after adding the background variation. JAVELIN is generally more sensitive to this for the lag uncertainties $\sigma_{\rm obs}$ and $\sigma_{\rm est}$, while ICCF, especially CCCD, is more sensitive to this for the median $(t_{\rm fit} - t_0)$.

In the second set of models, we randomly change the backgrounds in each trial while holding the standard deviation $\sigma_{\rm bkg}$ fixed. We show the results in the bottom two rows of Fig. 17. As expected, the medians of $(t_{\rm fit} - t_0)$ are generally closer to zero than in the fixed random seed cases. The observed scatter $\sigma_{\rm obs}$ increases significantly, while most of the estimated uncertainties $\sigma_{\rm est}$ changes only slightly. The ratio η drops as a result, and both algorithms underestimate the lag uncertainties except in a few cases for NGC 4593. As noted earlier, the linear parameters $\mathbf{L}\boldsymbol{q}$ in JAVELIN allows for the

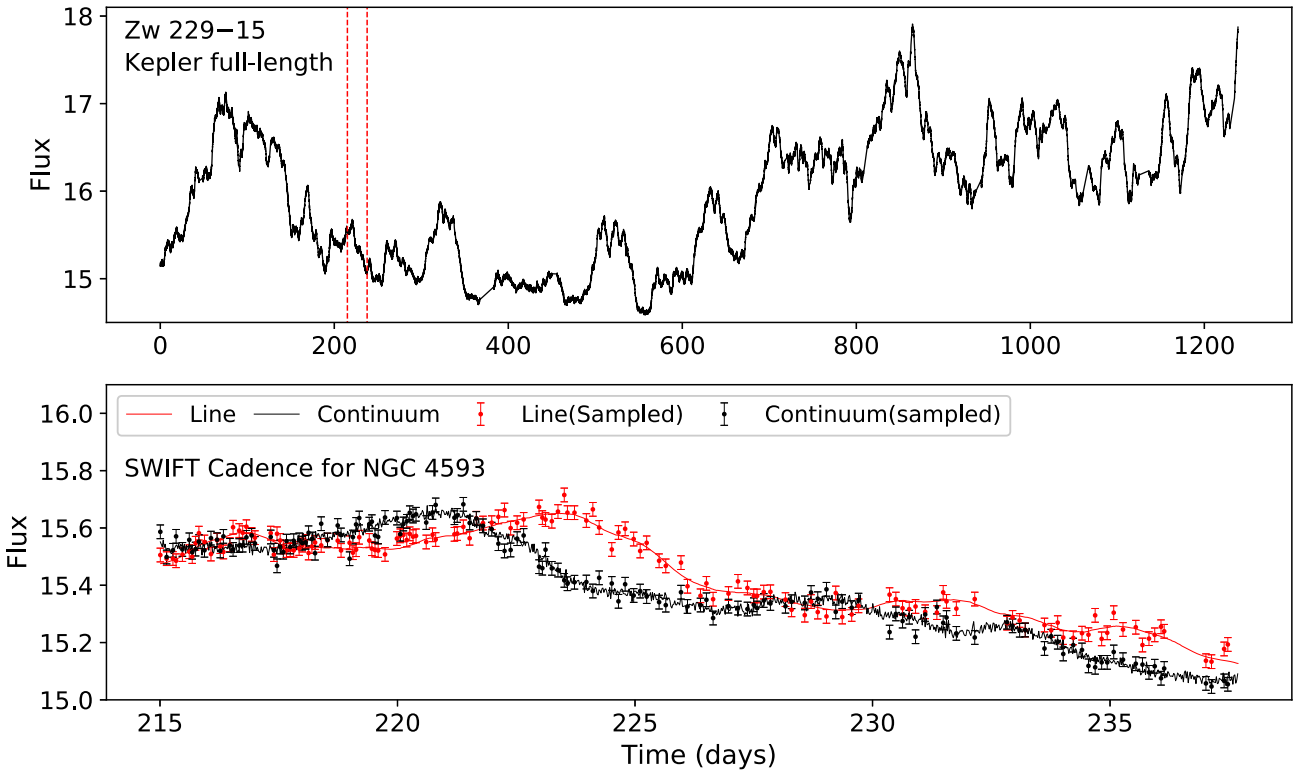

Figure 14. The top panel shows the *Kepler* light curve of Zw 229−15 from Edelson et al. (2014). We fill the observational gaps through linear interpolations. The bottom panel zooms in on the time interval between the red dashed lines in the top panel. The black solid line shows the observed *Kepler* light curve of Zw 229−15. The black points show the resampled *Kepler* light curve for the Swift cadence for NGC 4593 including noise. The red solid line shows an example of the simulated line light curves after convolving the *Kepler* light curve with a top-hat transfer function. The red points show the resampled line light curve using the fractional errors of the *Swift* data.

modelling of systematic trends. The trends can be different for the continuum and line light curves, allowing JAVELIN to handle the problem considered in this section as part of its analysis. However, an expansion of our analysis to fully explore these modifications is beyond our present scope.

4 DISCUSSION AND SUMMARY

We used observationally constrained simulated light curves to probe the effects of systematic errors on the JAVELIN and ICCF methods under a wide range of circumstances. We measured the lags from the simulated light curves through JAVELIN and ICCF and compared the input lag t_0 and the output lags $t_{\rm fit}$. We characterized the performance of the algorithms with the median $(t_{\rm fit} - t_0)$, the observed scatter $\sigma_{\rm obs}$, the estimated uncertainty $\sigma_{\rm est}$ and the ratio $\eta = \sigma_{\rm est}/\sigma_{\rm obs}$.

In general, we found that both methods are reasonably robust to the presence of all but one of the systematic problems we explored. In most circumstances, JAVELIN produces better lag error estimates in the sense that its error estimates are more consistent with the scatter of the results from random trials (i.e. the ratio η closer to unity). The ICCF method tends to overestimate the lag uncertainties. Because the ICCF method overestimates uncertainties when there are no severe systematic problems, it can be somewhat more 'robust' when there are severe systematic problems.

Incorrect single-epoch error estimates and correlated errors in the light curves can lead to incorrect lag uncertainties, but generally not by large factors unless there are very big problems. Because JAVELIN is explicitly Gaussian, its error estimates are directly affected by problems in the light-curve uncertainty estimates. If the true uncertainties are twice or half the uncertainties supplied to JAVELIN, it will get a lag uncertainty wrong by a factor of two simply because of its mathematical structure. Since the ICCF method does not explicitly depend on the single-epoch errors, the effects of the problems in the light-curve errors tend to be more subtle. Temporally correlated errors can have a bigger effect than the random errors, probably because they are effectively a distortion in the light-curve shape.

As previously found by Rybicki & Kleyna (1994) and Zu et al. (2013), changes in the shape of the transfer function have little effect on the lags. The primary exception is that a transfer function with a narrow peak and long tails will increasingly favour the lag due to the peak as the tail becomes longer. However, this effect was modest even for the 10:1 time-scale ratio we considered in our experiments.

As we would expect from the underlying mathematics of JAVELIN, it does not matter if the true stochastic process of the continuum light curves differs from the DRW model used by JAVELIN. We demonstrate this both with model light curves that have suppressed power on short time-scales and with empirical light curves from *Kepler* which show such modified structure functions. The performance of the ICCF method also shows no significant consequences from changes in the process driving the variability.

As noted in the Introduction, there are also many studies exploring how the algorithms perform as the cadence, temporal baseline and signal-to-noise ratio of the observations change, and address the likelihood of lag measurements for lower cadence light curves (e.g. Horne et al. 2004; King et al. 2015; Shen et al. 2015; Yu et al. 2019; I-Hsiu Li et al. 2019). The more recent studies generally find that

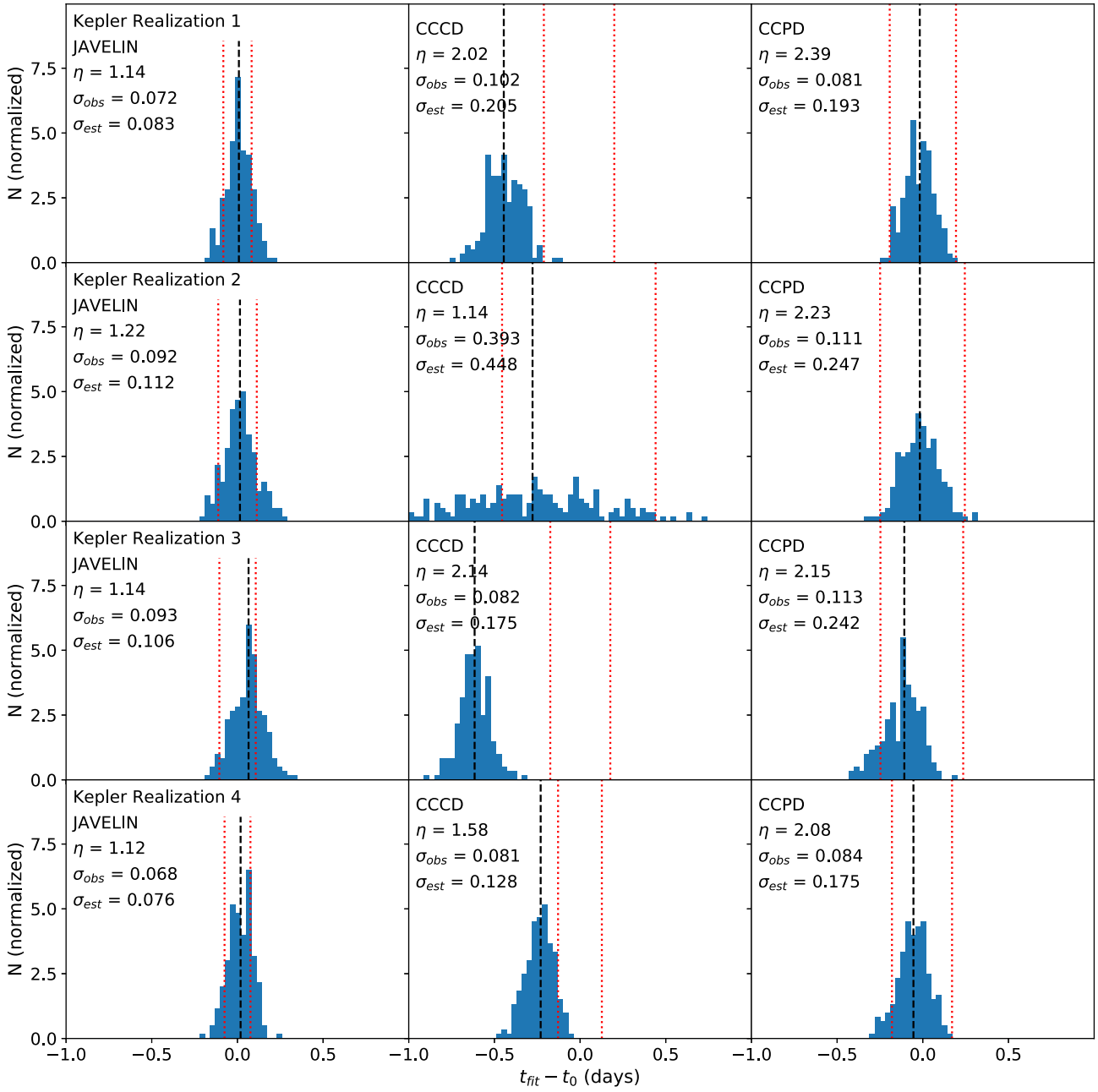

Figure 15. Same as Fig. 3, but for the simulated light curves based on the *Kepler* light curve of Zw 229−15. The first through the fourth rows show the results from each 'realization' of the *Kepler* light curves.

JAVELIN is more likely to yield an accurate lag measurement and, consistent with our results, that it generally provides more accurate lag uncertainty estimates. In general, however, these studies have generated their simulated light curves using JAVELIN's baseline assumptions, which is why we have focused on the consequences of violating those assumptions.

We do, however, identify one systematic problem which produces significant biases. The standard assumption of RM is that the line light curve is a smoothed and shifted version of the continuum (equation 1). If this assumption is incorrect, then both JAVELIN and ICCF begin to produce increasingly inaccurate lag estimates. We observe such effects after adding extra variability to the simulated light curves that resembles the anomalous variability found in NGC 5548. Such violations of the fundamental assumptions of RM are probably the dominant cause of problems in lag estimates from light curves which show variability features that should otherwise yield accurate lag measurements. We did not test combinations of multiple systematic errors because of the combinatoric explosion of cases. Mathematically there should be no surprises and the varying background effect will remain the most important source of systematic errors for both algorithms. While we discuss our results mostly in terms of the emission-line RM, they are equally applicable to continuum RM. The tests we performed for JAVELIN and ICCF can also be extended to other algorithms such as ZDCF and CREAM, or to the measurement of time delays in gravitational lenses (e.g. Liao et al. 2015) for prospective future studies.

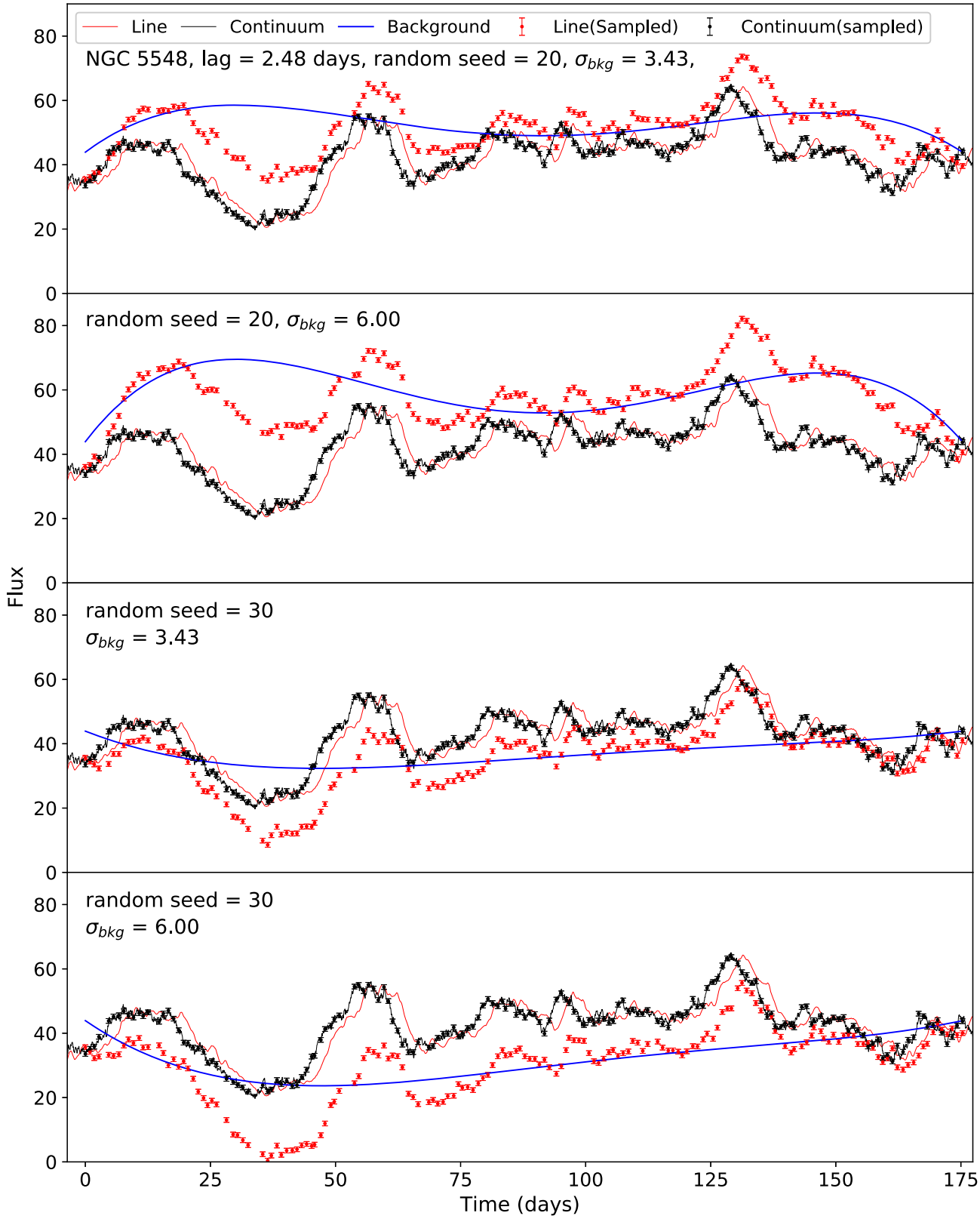

Figure 16. Simulated continuum and line light curves for NGC 5548 with a background variation. Each panel shows one model configuration with the parameters in the top left corner. The flux is in arbitrary units. The solid black and red lines represent the high-cadence simulated light curve of the continuum and the emission lines, respectively, while the black and red points represent the resampled light curves. The blue solid line represents the background level. The background variation is only included in the resampled line light curve.

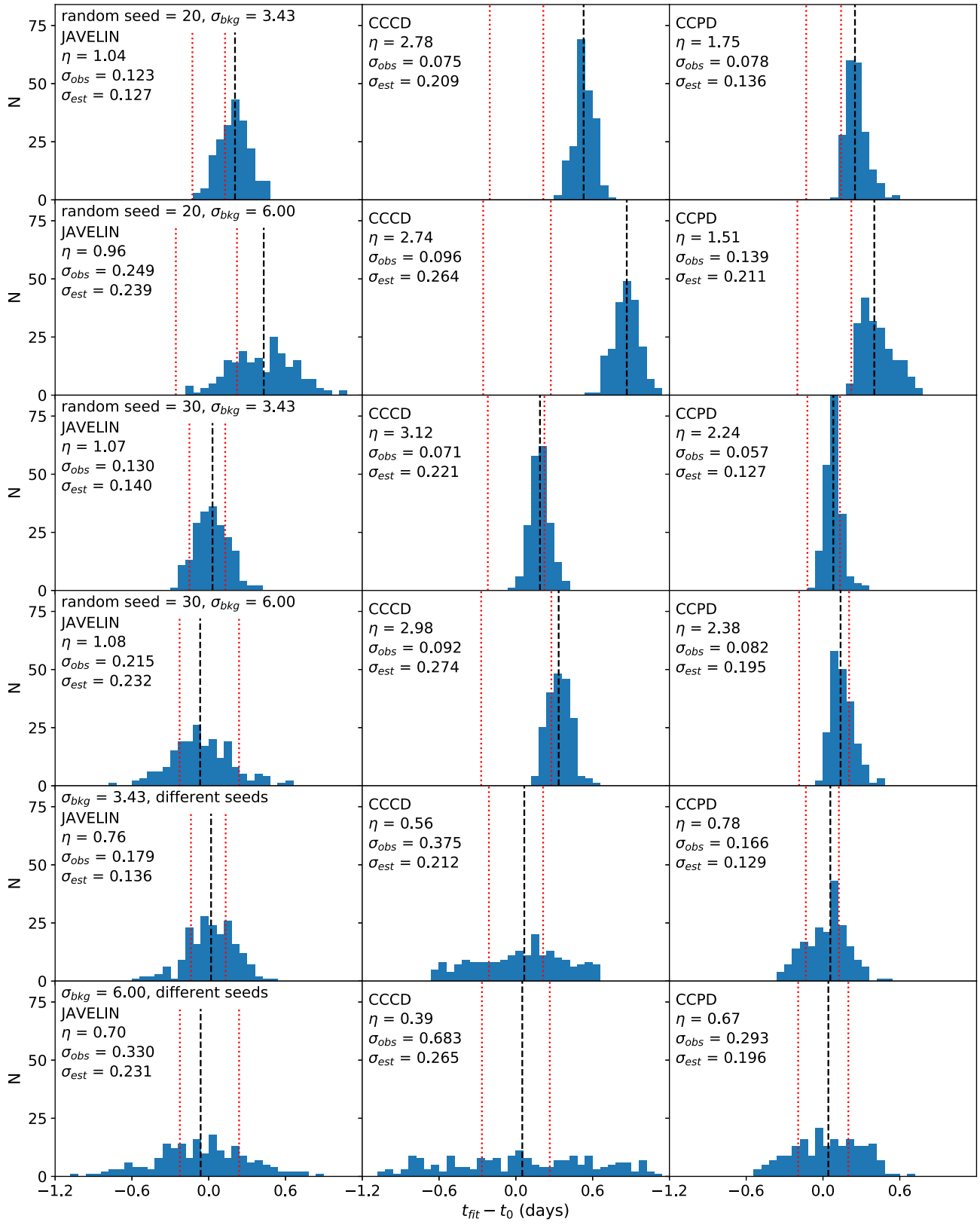

Figure 17. Same as Fig. 3, but for the results from background variations. Each panel shows the results from one model configuration with the parameters at the top left corner.

ACKNOWLEDGEMENTS

We thank the anonymous referee for the comments and suggestions on our paper. C.S.K. is supported by National Science Foundation (NSF) grants AST-1515876, AST-1515927, and AST-1814440. Z.Y. is supported by NSF under grant no. 1615553. E.M.C. gratefully acknowledges support from NSF grant AST-1909199. I.M.M. acknowledges support from Science and Technology Facilities Council (STFC) under grant ST/R000638/1.

REFERENCES

Alexander T., 1997, in Maoz D., Sternberg A., Leibowitz E. M., eds, Astrophysics and Space Science Library Vol. 218, Astronomical Time Series, Springer Netherlands, Tiergartenstrasse 17, Heidelberg, 69121, Germany. p. 163
Alexander T., 2013, preprint (arXiv:1302.1508)
Barth A. J., Boizelle B. D., Darling J., Baker A. J., Buote D. A., Ho L. C., Walsh J. L., 2016, ApJ, 822, L28
Bentz M. C. et al., 2013, ApJ, 767, 149
Blandford R. D., McKee C. F., 1982, ApJ, 255, 419
Cackett E. M., Chiang C.-Y., McHardy I., Edelson R., Goad M. R., Horne K., Korista K. T., 2018, ApJ, 857, 53
Czerny B., Olejak A., Ralowski M., Kozlowski S., Loli Martinez Aldama M. et al., 2019, ApJ, 880, 46
De Rosa G. et al., 2015, ApJ, 806, 128
Dehghanian M. et al., 2018, ApJ, 877, 119
Edelson R. A., Krolik J. H., 1988, ApJ, 333, 646
Edelson R., Vaughan S., Malkan M., Kelly B. C., Smith K. L., Boyd P. T., Mushotzky R., 2014, ApJ, 795, 2
Edelson R. et al., 2015, ApJ, 806, 129
Edelson R. et al., 2017, ApJ, 840, 41
Edelson R. et al., 2019, ApJ, 870, 123
Epitropakis A., Papadakis I. E., 2016, A&A, 591, A113
Fausnaugh M. M. et al., 2016, ApJ, 821, 56
Fausnaugh M. M. et al., 2017, ApJ, 840, 97
Gaskell C. M., Peterson B. M., 1987, ApJS, 65, 1
Gebhardt K., Thomas J., 2009, ApJ, 700, 1690
Goad M. R. et al., 2016, ApJ, 824, 11
Goad M. R. et al., 2019, MNRAS, 486, 5362
Grier C. J. et al., 2017, ApJ, 851, 21
Harms R. J. et al., 1994, ApJ, 435, L35
Homayouni Y. et al., 2018, ApJ, 880, 126
Horne K., Peterson B. M., Collier S. J., Netzer H., 2004, PASP, 116, 465
Horne K. D., De Rosa G., Peterson B. M., Barth A. J. , Ely J., et al., In Prep
I-Hsiu Li J. et al., 2019, ApJ, 884, 119
Jiang Y.-F. et al., 2017, ApJ, 836, 186
Johnson M. C., Cochran W. D., Collier Cameron A., Bayliss D., 2015, ApJ, 810, L23
Kasliwal V. P., Vogeley M. S., Richards G. T., Williams J., Carini M. T., 2015, MNRAS, 453, 2075
Kaspi S., Smith P. S., Netzer H., Maoz D., Jannuzi B. T., Giveon U., 2000, ApJ, 533, 631
Kelly B. C., Bechtold J., Siemiginowska A., 2009, ApJ, 698, 895
King A. L. et al., 2015, MNRAS, 453, 1701
Koen C., 1994, MNRAS, 268, 690
Kovačević A., Popović L. Č., Shapovalova A. I., Ilić D., Burenkov A. N., Chavushyan V. H., 2014, Adv. Space Res., 54, 1414
Kozłowski S. et al., 2010, ApJ, 708, 927
Kriss G. A. et al., 2019, ApJ, 881, 153
Krolik J. H., Done C., 1995, ApJ, 440, 166
Lewis T. O., Odell P. L., 1971, Estimation in Linear Models. Prentice-Hall, Upper Saddle River, NJ
Liao K. et al., 2015, ApJ, 800, 11
MacLeod C. L. et al., 2010, ApJ, 721, 1014
Matern B., 1960, Spatial Variation. Springer, Berlin
Mathur S. et al., 2017, ApJ, 846, 55
McHardy I. M. et al., 2018, MNRAS, 480, 2881
Mudd D. et al., 2018, ApJ, 862, 123
Mushotzky R. F., Edelson R., Baumgartner W., Gandhi P., 2011, ApJ, 743, L12
O'Hagan A., 1978, J. R. Stat. Soc. Ser. B (Methodol.), 40, 1
Peterson B. M., Pogge R. W., Wanders I., Smith S. M., Romanishin W., 1995, PASP, 107, 579
Peterson B. M., Wanders I., Horne K., Collier S., Alexander T., Kaspi S., Maoz D., 1998, PASP, 110, 660
Peterson B. M. et al., 2004, ApJ, 613, 682
Press W. H., Rybicki G. B., Hewitt J. N., 1992a, ApJ, 385, 404
Press W. H., Rybicki G. B., Hewitt J. N., 1992b, ApJ, 385, 416
Rao C. R., 1973, Linear Statistical Inference and its Applications, 2nd edn., Wiley, New York
Rybicki G. B., Kleyna J. T., 1994, in Gondhalekar P. M., Horne K., Peterson B. M., eds, ASP Conf. Ser. Vol. 69, Reverberation Mapping of the Broad-Line Region in Active Galactic Nuclei. Astron. Soc. Pac., San Francisco,p. 85
Rybicki G. B., Press W. H., 1992, ApJ, 398, 169
Shakura N. I., Sunyaev R. A., 1973, A&A, 24, 337
Shappee B. J. et al., 2014, ApJ, 788, 48
Shen Y. et al., 2015, ApJS, 216, 4
Shields G. A., 1978, Nature, 272, 706
Skielboe A., Pancoast A., Treu T., Park D., Barth A. J., Bentz M. C., 2015, MNRAS, 454, 144
Smith K. L., Mushotzky R. F., Boyd P. T., Malkan M., Howell S. B., Gelino D. M., 2018, ApJ, 857, 141
Starkey D. A., Horne K., Villforth C., 2016, MNRAS, 456, 1960
Sun M., Grier C. J., Peterson B. M., 2018, Astrophysics Source Code Library, record ascl:1805.032
Uttley P., Cackett E. M., Fabian A. C., Kara E., Wilkins D. R., 2014, A&AR, 22, 72
van der Marel R. P., 1994, MNRAS, 270, 271
Yu Z., Martini P., Davis T. M., Gruendl R. A., Hoormann J. K. et al., 2019, preprint (arXiv:1811.03638)
Zhang Y. H., 2002, MNRAS, 337, 609
Zu Y., Kochanek C. S., Peterson B. M., 2011, ApJ, 735, 80
Zu Y., Kochanek C. S., Kozłowski S., Udalski A., 2013, ApJ, 765, 106

SUPPORTING INFORMATION

Supplementary data are available at *MNRAS* online.

'figure_online.zip' includes result figures for NGC 4151, NGC 4593 and Mrk 509 that are not included in the main body of the paper. These figures have the same format as Fig. 3.

Please note: Oxford University Press is not responsible for the content or functionality of any supporting materials supplied by the authors. Any queries (other than missing material) should be directed to the corresponding author for the article.

This paper has been typeset from a TEX/LATEX file prepared by the author.